The JUICE 2024 close flyby of the Moon: Thermal assessment from MAJIS

Federico Tosi[1], Clément Royer[2], Federico Colaiuta[3,1], François Poulet[2], Tyler M. Powell[4], Benjamin T. Greenhagen[4], Yves Langevin[2], Alessandro Mura[1], Giuseppe Piccioni[1], Cédric Pilorget[2], Cristian Carli[1], Francesca Zambon[1]

[1]Istituto Nazionale di Astrofisica – Istituto di Astrofisica e Planetologia Spaziali (INAF–IAPS), Rome, Italy
[2]Institut d'Astrophysique Spatiale, CNRS/Paris-Saclay University, Paris, France
[3]University of Rome "La Sapienza", Department of Physics, Rome, Italy
[4]Johns Hopkins University – Applied Physics Laboratory (JHU–APL), Laurel (MD), USA

Correspondence to: Federico Tosi (federico.tosi@inaf.it)

Abstract. We present an analysis of four mid-infrared observations of the lunar surface acquired by the MAJIS instrument during the Jupiter Icy Moons Explorer (JUICE) gravity assist in August 2024. The data span 0.49–5.56 µm at sub-kilometre spatial resolution. These data provide a rare opportunity to investigate the challenging spectral regime where reflected solar radiation and thermal emission both contribute to the measured radiance.

The study explores three independent approaches to model and retrieve surface temperature and emissivity: (i) a Bayesian inversion framework, (ii) an empirical thermal correction method, and (iii) a roughness-informed thermophysical model. Rather than constituting a formal instrument validation, this paper provides a methodological consistency assessment of thermal retrieval strategies when applied to MAJIS mid-infrared data.

Retrieved temperature distributions are compared with expectations from established lunar thermal behaviour, and emissivity spectra are analysed in relation to known compositional contrasts between mare and highland terrains. The analysis highlights the sensitivity of the 3–5 µm crossover regime to modelling assumptions, temperature–emissivity coupling, and surface roughness parameterization.

Overall, the results demonstrate that MAJIS mid-infrared observations can be interpreted within physically consistent thermal modelling frameworks, while also revealing limitations and degeneracies inherent to this wavelength range. This workflow is directly transferable to future MAJIS observations of Jovian moons in the reflected–thermal crossover regime.

1 Introduction

The European Space Agency's JUpiter ICy moons Explorer (JUICE) mission (Grasset et al., 2013), launched in April 2023, executed a close lunar flyby in August 2024 as part of its interplanetary trajectory toward Jupiter. While JUICE is optimized for the exploration of Jupiter's icy satellites, this flyby provided a critical opportunity to assess the instrumental performance of the scientific payload within a well-characterized planetary environment. For the Moons and Jupiter Imaging Spectrometer

(MAJIS) (Poulet et al., 2024), this flyby served a dual purpose: assessing the performance of MAJIS data products and demonstrating its capability to retrieve physical and compositional surface properties under known lunar conditions at sub-kilometre spatial resolution and with unprecedented spectral resolution (Poulet et al., this issue). The present work is not intended as a formal, instrument-level validation of MAJIS. Topics such as absolute radiometric and spectral calibration (and its post-launch evolution), geometric calibration and pointing performance, and instrument thermal behaviour relevant to dark-signal subtraction and operability are addressed in dedicated companion papers (Langevin et al., this issue; Guerlet et al., this issue; Seignovert et al., this issue; Poulet et al., this issue, respectively). Although the modelling will provide a check of the absolute calibration of the IR channel, our focus is here on assessing the physical consistency and methodological robustness of thermal retrieval approaches applied to MAJIS mid-infrared observations of a well-characterized planetary surface.

Characterizing the Moon's surface thermal environment has been a long-standing scientific objective. Early ground-based and Earth-orbital telescopic observations provided bulk thermal properties and large-scale diurnal trends. The Apollo program acquired the first in situ heat flow measurements (e.g., Apollo 15, 17) and direct surface temperature records (Keihm et al., 1973; Keihm and Langseth, 1975). However, high-resolution orbital thermal mapping of the Moon only became routine with the Diviner Lunar Radiometer Experiment aboard NASA's Lunar Reconnaissance Orbiter (LRO) (Paige et al., 2010). Since 2009, Diviner has delivered near-global, multi-annual coverage of lunar surface temperatures at ~200 m/pixel resolution across multiple local times, enabling detailed studies of thermal inertia, rock abundance, rock size-frequency distributions, and volatile stability in permanently shadowed regions. Despite this revolutionary dataset, a significant observational gap remains in the near-infrared range 3.0–5.5 μm, where reflected sunlight and thermal emission overlap and where emissivity–temperature coupling is strongest. This interval thus complements the longer-wavelength coverage of Diviner, extending high-resolution thermal measurements into a spectral domain previously unexplored at global scales.

Prior to JUICE, the Moon had been observed by other imaging spectrometers, although none provided the combination of spatial resolution and spectral coverage needed for detailed thermal analysis. The Moon Mineralogy Mapper (M^3) onboard Chandrayaan-1 (Pieters et al., 2009) achieved near-global mineralogical mapping with a typical spatial resolution of 140 m/pixel but was limited to wavelengths shorter than 3 μm. The Visible and Infrared Mapping Spectrometer (VIMS) aboard Cassini (Brown et al., 2004) observed the Moon during its Earth swing-by in August 1999, mainly for the purpose of calibration. While VIMS covered wavelengths up to 5.1 μm, the data acquired during the lunar flyby suffered from both very coarse spatial resolution (~192 km/px) and severe saturation above 3.7 μm (Bellucci et al., 2002), which together precluded their use for any meaningful thermal mapping. Likewise, the JIRAM spectro-imager onboard NASA's Juno spacecraft (Adriani et al., 2017) acquired images and spectra of the Moon during the Earth flyby that occurred in October 2013, but with coarse spatial resolution (52–55 km/pixel), which enabled thermal retrieval in the range 3.0–4.2 μm mostly for the purpose of validating the instrument performances (Adriani et al., 2016). The Imaging Infrared Spectrometer (IIRS) on board Chandrayaan-2 (Chowdhury et al., 2020) acquired hyperspectral data of the Moon in the 0.8–5.0 μm range at a spatial resolution of approximately 80 m/pixel, demonstrating its capability to retrieve lunar surface temperatures and emissivity in the 3.0–5.0 μm range at local scale (Verma et al., 2022; Ojha et al., 2024). In addition, disk-resolved single-band mid-infrared

observations of the Moon at 3.5–4.1 μm (effective wavelength ~3.8 μm) were recently acquired by the geostationary Gaofen-4 satellite, providing a global reference for lunar radiance in the reflected–thermal crossover regime (Wu et al., 2021). More recently, the Moon was also observed in the thermal infrared during Lucy's 2022 Earth gravity assist with the L'TES instrument operating in the 5.8–100 μm spectral range, primarily as an in-flight calibration and validation target, providing high–spectral-resolution TIR spectra that are consistent with Diviner constraints and Apollo soil laboratory measurements (Christensen et al., 2025). MAJIS observations during the JUICE flyby provide a complementary dataset characterized by a distinct illumination geometry, with a broad spectral range extending from 0.49 to 5.56 μm, and a different instrumental heritage, allowing an independent consistency assessment of thermal retrieval approaches and offering new insights into the thermophysical properties of specific lunar regions under varying solar illumination.

On August 19, 2024, during the JUICE Lunar Gravity Assist (LGA), in the outbound leg of the flyby shortly after closest approach, MAJIS acquired four hyperspectral images of the lunar surface in the overall spectral range 0.49–5.56 μm. We tag these observations respectively: C1, C2, C3 and C4. Taken from altitudes of 874 to 2406 km over the surface, these datasets yielded average pixel scales between 0.13 and 0.36 km/pixel, providing exceptional sub-kilometre infrared coverage across varying incidence angles and local times (a detailed description of the MAJIS data and the flyby geometry is documented in Poulet et al., this issue). Table 1 summarizes key specifications of the MAJIS LGA data. In the C4 observation, the first 17 out of 64 pixels along the slit ("*samples*") are not usable because the observation was purposely commanded to illuminate only part of the slit to evaluate the magnitude of straylight; therefore, they are ignored in the subsequent thermal analysis.

Table 1. Main features of the four hyperspectral images acquired by MAJIS during the JUICE flyby of the Moon on August 19, 2024.

	C1	**C2**	**C3**	**C4**
Filename	20240819211816	20240819211923	20240819212141	20240819212402
Start time (UTC)	2024-08-19T21:18:16	2024-08-19T21:19:24	2024-08-19T21:21:42	2024-08-19T21:24:02
Stop time (UTC)	2024-08-19T21:19:06	2024-08-19T21:21:31	2024-08-19T21:23:49	2024-08-19T21:25:26
Size (samples × lines × bands)	400 × 99 × 1016	64 × 1274 × 1016	64 × 1269 × 1016	64 × 841 × 1016
Altitude over the surface (km)	873.95 – 942.45	971.52 – 1269.24	1286.80 – 1813.27	1791.97 – 2406.05
Pixel resolution (km)	0.131 – 0.141	0.146 – 0.190	0.193 – 0.272	0.269 – 0.361
Phase angle (deg)	88.5 – 91.9	89.9 – 90.5	89.9 – 90.5	88.4 – 88.9
Solar incidence angle (deg)	85.0 – 93.1	66.2 – 83.7	44.4 – 65.2	26.3 – 45.1
Emission angle (deg)	0.2 – 7.0	8.2 – 26.0	25.2 – 47.9	43.4 – 65.7
Local solar time (h)	17.6 – 18.2	16.4 – 17.6	15.0 – 16.3	13.7 – 15.0

The JUICE/MAJIS flyby data complement the legacy of Diviner in two key ways: (1) they achieve spatial resolution comparable to Diviner during a targeted campaign, and (2) they extend high-resolution coverage into the 3.0–5.56 μm infrared spectral domain, which is under-explored for the Moon. Unlike Diviner's broadband and multispectral thermal infrared (TIR) channels, MAJIS provides hyperspectral coverage across the 2.28–5.56 μm range with an average ~7-nm spectral resolution (Haffoud et al., 2024). This interval captures the Wien tail of thermal emission and may include weak overtone or combination features of silicate materials. The hyperspectral capability enables the simultaneous retrieval of brightness temperature and spectral emissivity with high fidelity. Such data reveal subtle variations diagnostic of surface properties including roughness, regolith grain size, porosity, and composition—parameters that are often difficult to disentangle using broadband measurements.

Making the most of this small but novel dataset, the primary scientific objectives of the MAJIS lunar observations are: (1) to map diurnal temperature variability at high spatial resolution, (2) to retrieve spectral emissivity longward of 3 μm, and (3) to assess thermophysical properties where constrained by observation geometry. While the single flyby precludes broad-scale thermal inertia mapping, the hyperspectral data enable targeted thermophysical insights at specific locations. Localized modelling—leveraging distinct observation geometries, known crater morphology, and predicted self-heating effects—allows quantification of surface roughness at sub-kilometre scales. Furthermore, spectral emissivity retrievals provide independent constraints on regolith texture (grain size, packing) intrinsically linked to thermophysical behaviour. These point estimates offer valuable validation against Diviner regional trends and in situ data.

Although the present analysis focuses on lunar observations, its relevance to the JUICE main mission lies primarily at the methodological level. The 3.0–5.5 μm spectral region investigated here corresponds to the crossover domain where reflected solar radiation and thermal emission coexist. The stability of temperature–emissivity separation in this regime, as well as the sensitivity of the inversion to prior assumptions, are largely independent of the specific target body and instead governed by radiative transfer physics and signal-to-noise characteristics.

In the Jovian system, this crossover regime is expected to be particularly relevant for Callisto, where the subsolar temperature value is approximately 165 K (Tosi et al., 2024, and references therein), allowing thermal emission to become detectable toward the long-wavelength edge of the MAJIS range (5.0–5.56 μm) (Royer et al., 2025). Ganymede may present a weaker but still measurable thermal contribution under favourable conditions, whereas Europa will likely represent a reflection-dominated case. While the physical parameters (albedo, emissivity spectra, thermal inertia, and surface roughness) must be adapted to icy regoliths, the inversion architecture and thermophysical modelling framework tested here remain directly applicable.

In the remainder of this paper, Section 2 presents the derivation of surface temperature and emissivity from MAJIS data using three independent approaches: (i) a Bayesian nonlinear inversion constrained by radiative transfer, (ii) an empirical thermal correction adapted from laboratory-based relationships, and (iii) a roughness-informed, physically consistent thermal model. Before intercomparing these methods, we introduce a cross-wavelength context by incorporating co-located LRO/Diviner observations to establish an external benchmark for both temperature and emissivity (subsection 2.4). We then evaluate the

performance of the three approaches in terms of their ability to reproduce observed thermal behaviour and emissivity contrasts across different terrains (subsection 2.5). Finally, in Section 3 we synthesize these results in a broader scientific discussion, drawing conclusions on the thermophysical properties of the lunar surface and outlining the implications for future applications of MAJIS to airless bodies in the outer Solar System.

2 Derivation of surface temperature and emissivity from MAJIS data

2.1 Bayesian approach to nonlinear inversion

The Bayesian nonlinear inversion used for MAJIS temperature retrieval builds upon techniques previously validated across multiple planetary missions. This methodology was routinely used on data acquired by the Dawn/VIR imaging spectrometer, which achieved nearly global coverage at asteroid Vesta and dwarf planet Ceres, leveraging the nonlinear radiance-temperature relationship to infer thermophysical properties while accommodating rapid rotational cycles (Tosi et al., 2014; Capria et al., 2014; Tosi et al., 2015; Tosi et al., 2018). The methodology's adaptability was further demonstrated on infrared data acquired by Rosetta/VIRTIS at the asteroid Lutetia (Keihm et al., 2012) and especially at the nucleus of comet 67P/Churyumov–Gerasimenko, resolving self-heating phenomena within shadowed concavities and diurnal thermal gradients at 15 m/pixel resolution (Tosi et al., 2019). Most directly, a similar Bayesian workflow was applied to JIRAM data of the Moon acquired during the 2013 Earth flyby of Juno to derive temperatures validated against LRO/Diviner data (Adriani et al., 2016).

The details of the Bayesian approach to nonlinear inversion are explained in the Appendix A of Tosi et al. (2014). Briefly, this technique addresses the inherent challenge of solving for multiple unknowns—temperature and wavelength-dependent emissivity—from a limited set of spectral radiance measurements. For a retrieval involving N spectral channels, the state vector includes N emissivity values plus the surface temperature, for a total of $N + 1$ free parameters.

The method follows the classical maximum-a-posteriori (MAP) formulation of Rodgers (2000), solved iteratively using a Gauss–Newton scheme. The radiative transfer model is linearized around an initial a priori state, and the optimal solution is obtained by minimizing a quadratic cost function combining the spectral misfit and the prior constraints. The associated posterior covariance matrix—derived from the inverse of the approximate Hessian of the cost function—provides the formal uncertainties of the retrieved parameters. In our implementation, the observation error covariance matrix S_e is defined using the in-flight Noise Equivalent Spectral Radiance (NESR) of MAJIS. In the absence of a validated model for channel-to-channel noise correlations, S_e is assumed diagonal, with wavelength-dependent variances given by the squared NESR. The a priori covariance matrix S_a applies soft constraints on temperature (±30 K) and on emissivity, enforcing physically plausible values ($\varepsilon \leq 1$) and spectral smoothness. In the present implementation, no a priori cross-covariances are prescribed between temperature and emissivity, and S_a is taken as diagonal. Temperature and emissivity are therefore constrained independently in the prior, while their coupling arises through the forward model and is reflected in the posterior covariance. Emissivity correlations between neighbouring spectral channels are represented through off-diagonal terms in S_a, modelled with a Gaussian correlation function: for spectral channels i and j at wavelengths λ_i and λ_j, we set:

$$cov(\varepsilon_i, \varepsilon_j) = \sigma_{\varepsilon i} \cdot \sigma_{\varepsilon j} \cdot e^{\frac{-(\lambda_i - \lambda_j)^2}{l^2}} \qquad i, j = 1 \ldots N \tag{1}$$

where $\sigma_{\varepsilon i}$ is the a priori standard deviation assigned to emissivity at channel i and l is the correlation length (chosen comparable to the spectral sampling, in our case 20 nm which is about three MAJIS-IR spectral channels). This regularization mitigates the intrinsic temperature–emissivity degeneracy, especially near the crossover region where reflected and emitted components are comparable, and stabilizes the emissivity solution while preserving physically plausible variability (Rodgers, 2000).

The physical basis of the approach lies in the radiance equation for airless bodies, where the measured spectrum combines reflected solar and thermally emitted radiation. At thermal equilibrium, Kirchhoff's law states that the spectral directional emissivity equals the corresponding spectral directional absorptivity. For an opaque surface (negligible transmittance), this can be written as $\varepsilon_d(\lambda)=1-r_{hd}(\lambda)$, where r_{hd} is the hemispherical–directional spectral reflectance. In the Bayesian retrieval, emissivity is treated as a spectral (channel-by-channel) directional quantity; no bolometric Kirchhoff relation is assumed. However, the system remains underconstrained without additional prior information. The inversion therefore begins with an estimate of surface temperature obtained from the brightness temperature in the dominant thermal-emission region, assuming an initial constant emissivity. An important refinement is the dynamic determination of the crossover wavelength—the point at which reflected and emitted radiation are equal—based on this temperature estimate. The spectral domain used in the inversion is then defined as extending from 0.5 µm shortward of this crossover to the long-wavelength limit of MAJIS sensitivity, ensuring that the crossover region is always included for a stable emissivity solution.

Priors constrain the physically meaningful variability of the unknowns (±30 K for temperature, and wavelength-dependent bounds on emissivity to ensure $\varepsilon \leq 1$ and avoid nonphysical solutions). In practice, these values represent soft constraints: they define the width of the a priori covariance matrix but do not impose hard limits. The Gauss–Newton iterations may therefore converge outside these ranges if supported by the radiance data. Only two hard constraints are applied. First, emissivity values exceeding unity are clipped to $\varepsilon = 1$. Second, spectral segments are discarded when the retrieved emissivity is inconsistent with Kirchhoff's law by more than 4%, i.e. when $r(\lambda)=1-\varepsilon(\lambda)$ indicates non-physical behaviour near the crossover region. These steps prevent non-physical behaviour while preserving the flexibility inherent in the Bayesian formulation. Formal uncertainties of temperature and emissivity are computed from the posterior covariance and incorporate the in-flight NESR, which increases toward longer wavelengths due to spectrometer background.

A Bayesian formulation offers significant advantages over a simple least-squares fit when estimating temperatures from infrared spectra, particularly when the available wavelengths lie in the Wien tail of the Planck function. In this regime, radiance depends exponentially on temperature, creating a strong degeneracy between temperature and emissivity and making least-squares solutions highly sensitive to noise and to the choice of initial emissivity. In practice, this ambiguity becomes stronger when the Jacobian sensitivities of the radiance to temperature and emissivity are similar, especially in the reflected/thermal crossover regime. In the present framework, this degeneracy is regularized through the covariance structure imposed on the

emissivity spectrum, which enforces smoothness across adjacent wavelengths while allowing physically plausible variability. Although the Gauss–Newton implementation retrieves only the local posterior maximum rather than the full posterior distribution, the posterior covariance naturally provides formal uncertainties that reflect the structure of the inverse problem. It is therefore used here to diagnose the uncertainties and correlations of the retrieved state, rather than to impose a prior relationship between temperature and emissivity. By suppressing unrealistic high-frequency oscillations—especially near the reflected/thermal crossover—the covariance-based regularization stabilizes the solution without imposing mineralogical assumptions.

Compared to approaches that fit a Planck function with a single emissivity value, the Bayesian retrieval therefore uses the covariance-based prior to regularize the temperature–emissivity degeneracy in a physically motivated way. Tighter spectral correlations suppress noise more efficiently but increase the risk of over-regularization, whereas looser correlations allow greater variability at the expense of stability.

Subsequent iterations refine temperature and emissivity simultaneously. For each pixel, the algorithm iterates up to 50 times, recalculating the Jacobian matrix (radiance sensitivity to parameter changes) at each step to update the solution and its uncertainties. Post-retrieval validation removes emissivity data affected by saturation or inconsistent with the Bayesian solution, ensuring robustness. The method achieves convergence even with suboptimal initial guesses, yielding reliable results for temperatures >170 K (the exact limit depends on sensitivity range and instrument thermal conditions) for dayside measurements. Typical formal uncertainties are 1–3 K for temperature in well lit areas and 0.01–0.20 for emissivity, increasing for low-temperature and/or high incidence angle scenarios.

For MAJIS, the heritage methodology was systematically adapted to lunar conditions. First, we consider data acquired only in the infrared (IR) channel, which covers the spectral range 2.28–5.56 µm. Raw data underwent reinsertion of the background signal (which is automatically subtracted in the calibration pipeline) to identify saturation artifacts, which appear as plateaus in the spectral profile, sometimes with oscillations. Spectral pixels ("*spectels*") exceeding 10,400 Digital Numbers (DN)—a threshold empirically derived from C4 data, which experience the highest solar illumination—were flagged and excluded. Synthetic radiance spectra were generated by combining thermal emission with reflected solar components modelled using the MODTRAN Cebula+Kurucz extraterrestrial solar spectrum (https://www.nrel.gov/grid/solar-resource/spectra.html) scaled for the heliocentric distance of the Moon at the time of the observation (1.014 au). Several hypotheses on the initial emissivity (0.70–0.95) were evaluated, and the initial temperature was set equal to the brightness temperature in the 5.27–5.56 µm range, allowing both parameters to vary within noise constraints until convergence. Two spectral ranges were tested: the computationally efficient 4.5–5.56 µm window (Table A1) and the broader 3.0–5.56 µm interval (Table A2), the latter reducing saturation biases in high-temperature regions at the cost of increased processing load. We treat this as a stability–information trade-off: the wider range increases leverage but also amplifies calibration/reflectance sensitivities in the crossover domain. The Lommel–Seeliger disk function (Hapke, 1981)—a photometric law optimized for the Moon—was also tested to account for illumination and viewing geometry (Table A3).

Geometric precision was ensured through SPICE kernel navigation data (Acton, 1996; Acton et al., 2018) and instrument kernels, defining ellipsoid-level planetocentric coordinates as well as solar incidence and emission angles. The LEGA observations enable an update of the MAJIS instrument kernel, with details provided in a companion paper dedicated to the geometric calibration (Seignovert et al., this issue). Topographic effects could in principle be mitigated using a digital elevation/shape model to compute local illumination and emission angles; however, no DEM-based topographic correction is applied in this work. While such corrections are critical for irregular bodies (e.g. asteroids and cometary nuclei), approximating the Moon as a smooth ellipsoid is adequate for the large-scale interpretation of MAJIS data at a spatial resolution of a few hundred metres per pixel. On the other hand, this approximation does not capture unresolved local slopes and shadowing, which may contribute to pixel-scale discrepancies. Emissivity outputs were restricted to the spectral range used for temperature retrieval (4.5–5.56 μm and 3.0–5.56 μm).

Using the range 4.5–5.56 μm, the temperature values obtained through the Bayesian inversion across the four MAJIS lunar observations (C1 to C4) reveal systematic dependencies on both the level of solar illumination and the choice of prior emissivity. As expected, the mean surface temperature increases from C1 through C4, reflecting progressively stronger solar heating (Figures 1–2). C1, acquired under grazing illumination, shows the lowest mean temperatures (~176–184 K), while C4, obtained under near-equatorial midday conditions, yields mean temperatures approaching 356–343 K, depending on the emissivity prior (Figure 3 and Table A1). To quantify the dependence of the retrieval on the emissivity prior, we evaluate the spread of the retrieved mean temperatures obtained using ε_0 = 0.70, 0.80, 0.90, and 0.95 (Table A1). For the 4.5–5.56 μm retrieval window, the mean temperature varies by $\Delta T\_mean \approx$ 8.6 K (C1), 2.2 K (C2), 9.2 K (C3), and 12.9 K (C4) across the tested priors. This confirms that the sensitivity to ε_0 is generally limited for intermediate illumination conditions (C2), whereas it becomes more significant under extreme thermal regimes, where the radiance–temperature relationship is strongly nonlinear and temperature–emissivity degeneracy is enhanced.

Representative signal-to-noise conditions for two example pixels (optimal and sub-optimal) are illustrated in Figure A1, where the measured radiance ± NESR is shown on the same radiance scale for reference, and the corresponding median signal-to-noise ratio (SNR) and 5–95% SNR range are reported explicitly.

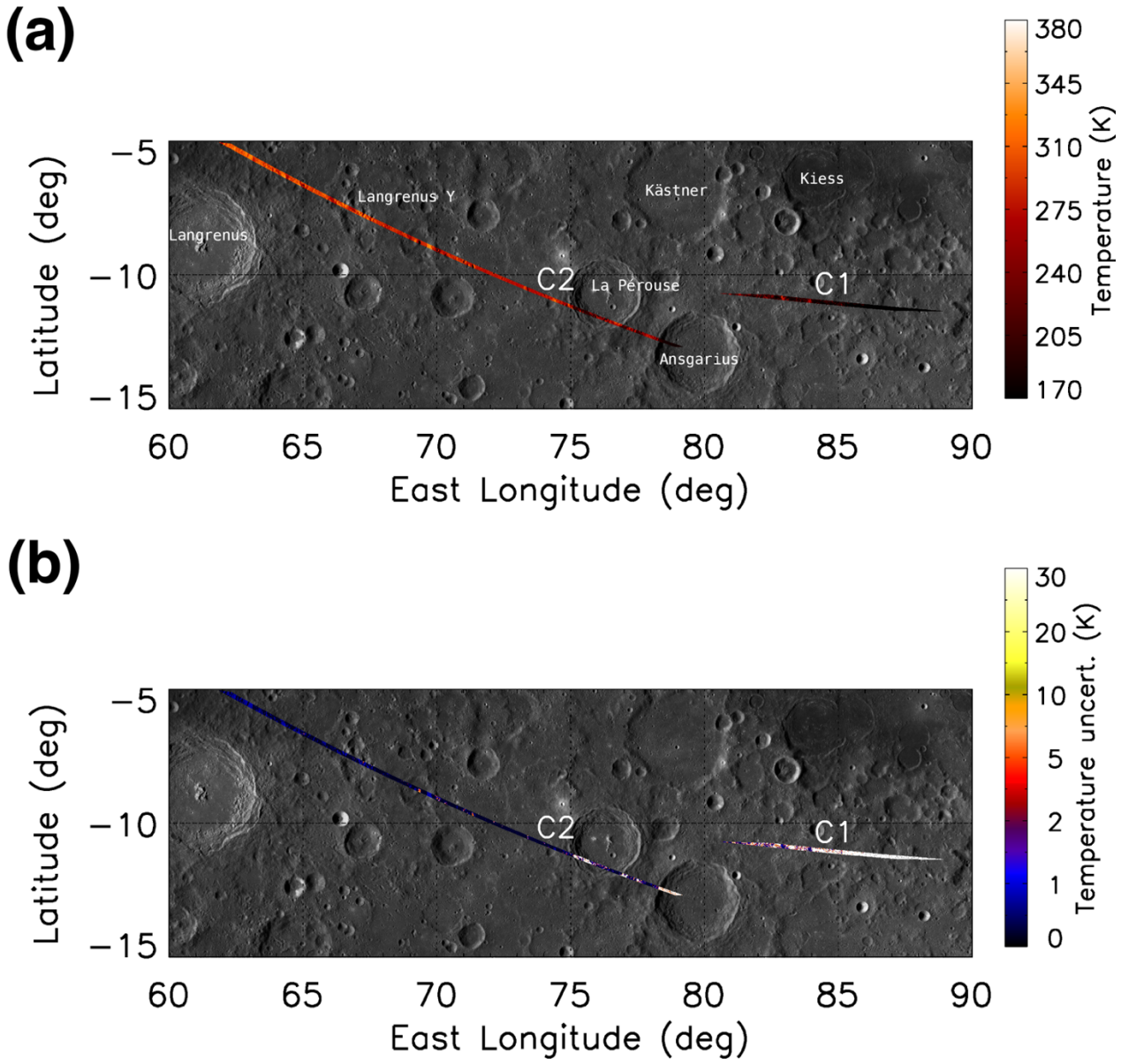

245

Figure 1. Bayesian temperature retrievals (C1–2). (**a**) Temperature maps derived from MAJIS observations C1 and C2, using the Bayesian approach applied to the 4.5–5.56 µm portion of the IR data using an emissivity prior of 0.70 ± 0.15 and no photometric correction. C1 is the easternmost data, taken near the terminator. C2 extends from northwest to southeast at low southern latitudes. Both data cover lunar highlands. Pixel resolution goes from 0.19 to 0.36 km. Colour gradation is mainly due to instantaneous solar illumination combined with
250 local topography. (**b**) Formal uncertainties associated with the retrieved temperature values. The largest uncertainties are associated with the lowest temperature values, corresponding to unlit locations. Background image: Moon LRO LROC WAC Global Morphology Mosaic 100m, June 2013 (Speyerer et al., 2011; Wagner et al., 2015).

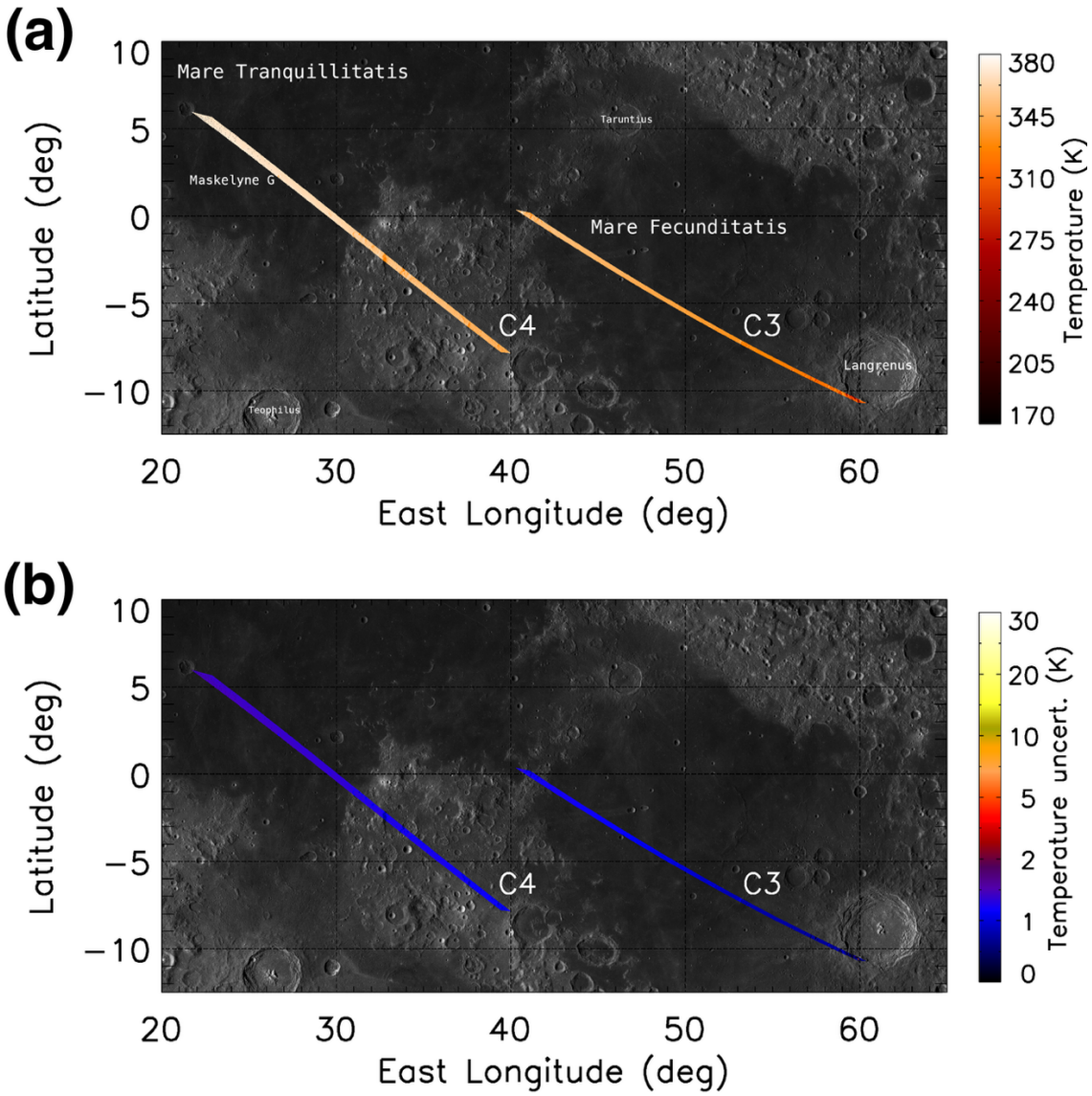

Figure 2. Bayesian temperature retrievals (C3–4). (**a**) Temperature maps derived from MAJIS observations C3 and C4, using the Bayesian approach applied to the 4.5–5.56 μm portion of the IR data under an emissivity prior of 0.70 ± 0.15 and no photometric correction. C3 is the easternmost data and mostly covers Mare Fecunditatis, bordering Langrenus crater in the southeastern edge. C4 is the westernmost data and embraces Mare Tranquillitatis and highlands in between Tranquillitatis and Fecunditatis. Both data extend from northwest to southeast at low southern latitudes, crossing the equator. Pixel resolution goes from 0.13 to 0.19 km. The colour gradation reaches its maximum on the scale, about 380 K, at the westernmost points of C4, which experience early afternoon. (**b**) Formal uncertainties associated with the retrieved temperature values. Typical average uncertainty is ~1 K. Background image: Moon LRO LROC WAC Global Morphology Mosaic 100m, June 2013 (Speyerer et al., 2011; Wagner et al., 2015).

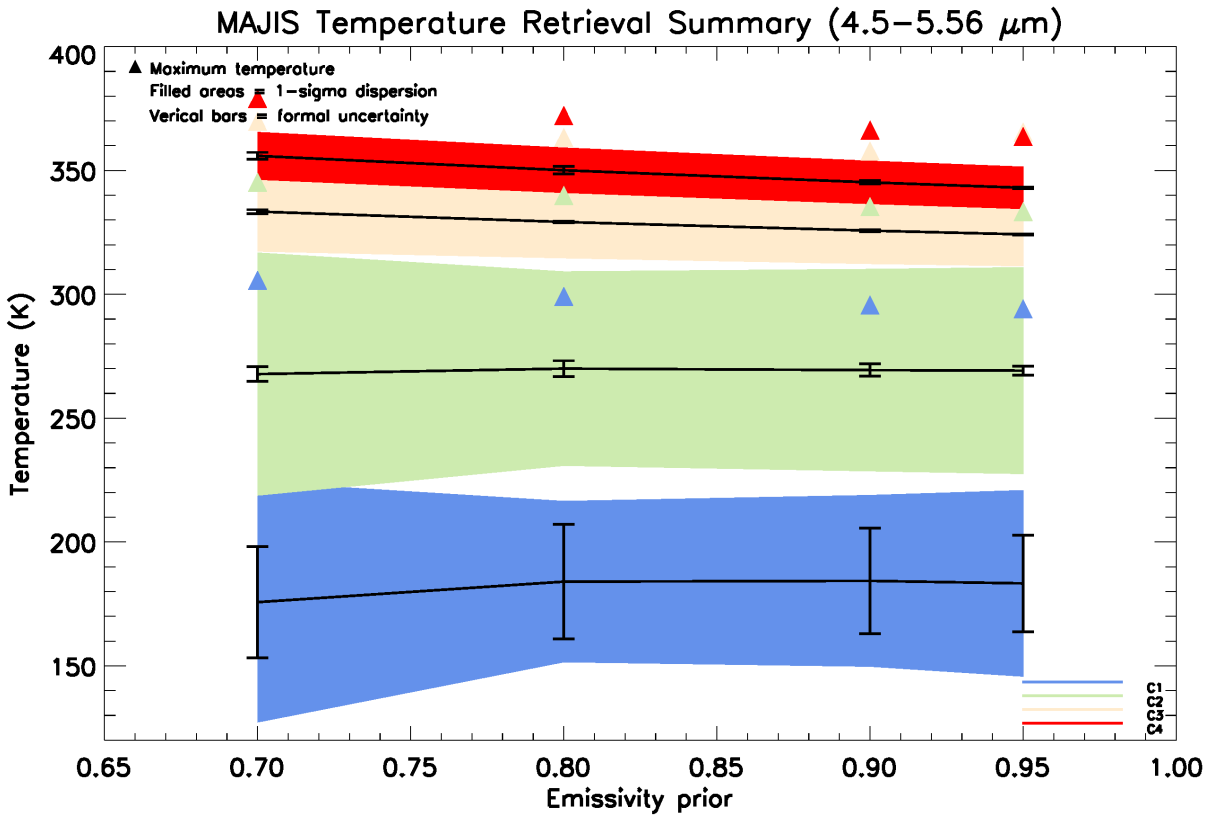

Figure 3. Summary of MAJIS temperature retrievals as a function of emissivity prior (4.5–5.56 µm spectral range). The coloured bands represent the retrieved mean surface temperature (solid lines) and the corresponding $\pm 1\sigma$ dispersion for the four MAJIS observations (C1–C4). Vertical black bars indicate the formal uncertainties associated with the Bayesian inversion, while triangles mark the maximum temperature values observed within each dataset. The results illustrate the sensitivity of the retrieved temperature to the assumed emissivity: for the warmer datasets (C3 and C4), the mean temperature decreases slightly with increasing emissivity prior, while for the colder, high incidence cases (C1 and C2) the dependence on the emissivity prior is weak and does not follow a strictly monotonic trend. Small, irregular variations with prior reflect low thermal signal, local illumination/topography and retrieval noise rather than a systematic physical response.

As expected, the choice of initial emissivity (ε_0) influences the retrieved temperatures. Lower assumed emissivity values yield higher temperature estimates, due to the inverse relationship between emissivity and brightness temperature in the Planck function. In high-SNR observations such as C4, this leads to differences in mean temperature as large as 13 K across the range of tested priors. In contrast, datasets acquired at higher incidence angles (e.g., C1 and C2) exhibit smaller temperature shifts across priors, likely because shadowed regions dominate the radiance signal, flattening the temperature distribution and dampening the sensitivity to ε_0.

The uncertainties associated with the retrieved temperatures show a more pronounced dependence on both solar illumination and the width of the emissivity prior. Formal uncertainties and 1–σ dispersions are significantly higher in C1 and C2, particularly when using broad priors (e.g., $\varepsilon_0 = 0.70 \pm 0.15$), reflecting the limited thermal contrast and stronger model degeneracy under low radiance conditions. In contrast, observations with higher insolation—namely C3 and C4—yield markedly lower formal errors and temperature dispersion. This reduction in spread is not only a function of radiometric quality but also of scene illumination: in C4, the entire observed area is well lit, and the few remaining shadows are due solely to local topography. This homogeneity in thermal forcing minimizes temperature variability across the scene and enhances retrieval precision, reinforcing the robustness of the Bayesian approach under favourable conditions.

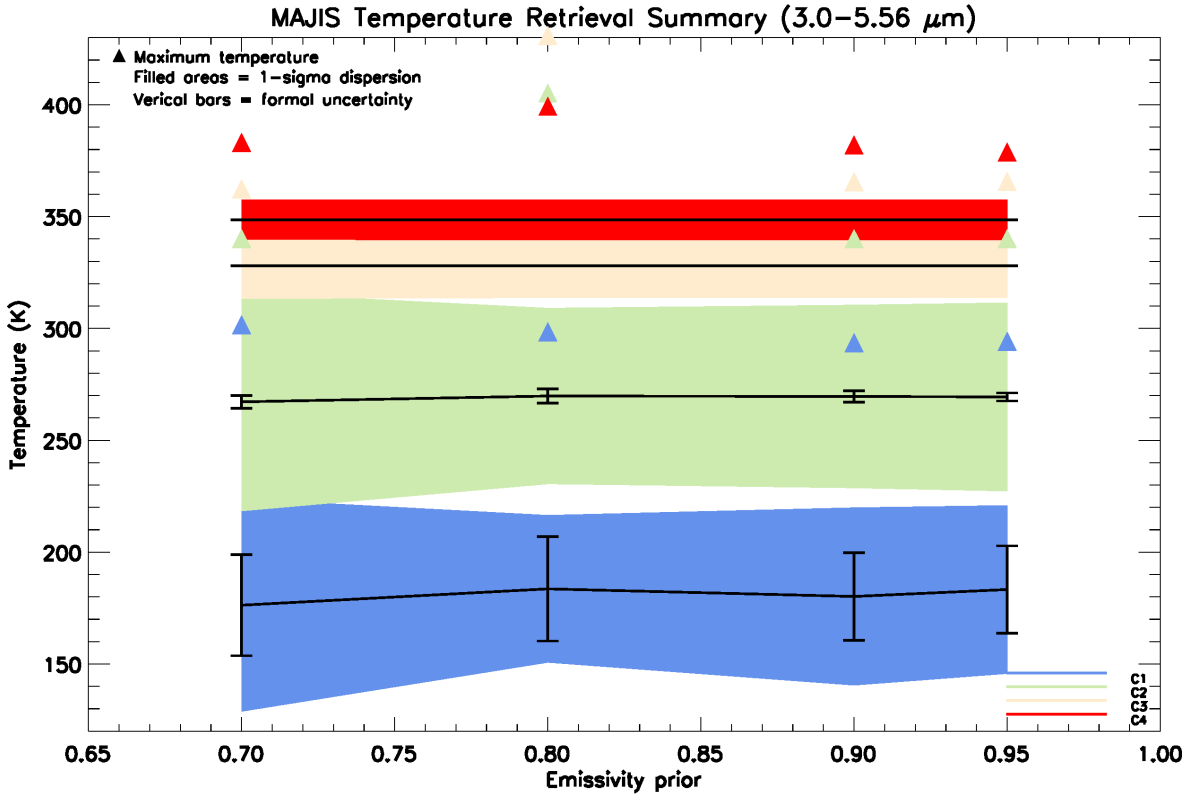

Figure 4. Summary of MAJIS temperature retrievals as a function of emissivity prior (3.0–5.56 µm spectral range). The coloured bands show the mean surface temperatures (solid lines) and corresponding ±1σ dispersion for the four MAJIS observations (C1–C4), obtained from Bayesian inversion without photometric correction. Vertical black bars represent the mean formal uncertainties, and triangles indicate the maximum retrieved temperature values. Compared with the 4.5–5.56 µm case, the wider spectral interval yields similar temperature trends but generally lower formal uncertainties, especially under well illuminated conditions.

Results show that extending the lower bound of the spectral window from 4.5 to 3.0 µm produces a significant change in the character of the inversion (Figure 4 and Table A2). When using the full 3.0–5.56 µm range, the retrieval yields temperature values that are nearly invariant with respect to the emissivity prior, especially in the well illuminated datasets C3 and C4. In these cases, the mean surface temperatures converge to a fixed value regardless of the prior, and, while the associated 1–σ dispersion is substantially similar to the 4.5–5.56 µm case, the formal uncertainties collapse to zero, indicating that the inversion algorithm has converged to a narrow solution space (Figure 5). Although such tight convergence might suggest improved precision, it more likely reflects numerical over-constraint. This behaviour is consistent with an over-dominant contribution from shorter wavelengths—between 3.0 and 4.2 µm—where thermal emission is still weak and the radiance spectrum is more sensitive to the shape of the assumed reflectance curve and potential calibration uncertainties.

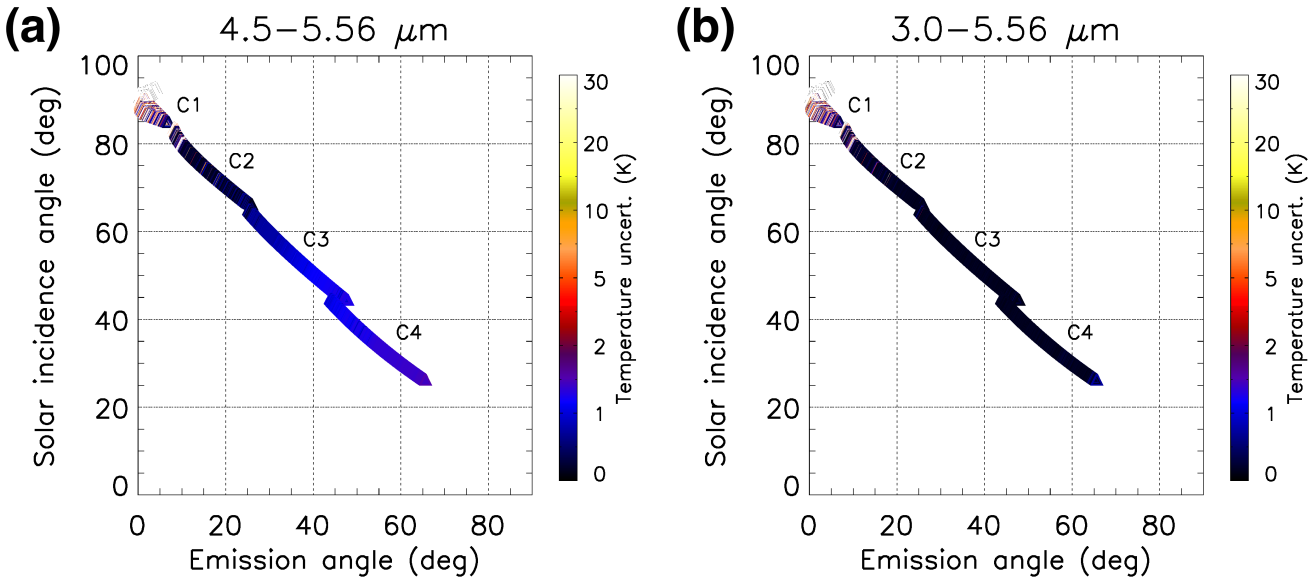

Figure 5. Formal uncertainties vs geometry. Formal uncertainties associated with the temperature values calculated in the four MAJIS acquisitions, as a function of the solar incidence angle (*y*-axis) and the emission angle (*x*-axis). Panels (**a**) and (**b**) refer to the retrieval cases in the range 4.5–5.56 µm and 3.0–5.56 µm, respectively. It can be noted that the wider spectral range results in a lower formal uncertainty under the same illumination and observation conditions for those data that benefit from full solar illumination.

Comparing corresponding rows across Tables A1 and A2 shows systematic differences in mean temperatures. For example, in C4 under $\varepsilon_0 = 0.90 \pm 0.10$, the mean temperature increases from 345.2 K (4.5–5.56 µm) to 348.6 K (3.0–5.56 µm), while in C1 it decreases from 184.3 K (4.5–5.56 µm) to 180.2 K (3.0–5.56 µm). These small shifts reflect the different spectral leverage of the two wavelength ranges, as shorter wavelengths provide enhanced sensitivity to the thermal continuum at higher temperatures. In warm, well illuminated conditions, the additional thermal signal from the 3.0–4.5 µm interval strengthens the

fit to the observed radiance, improving the stability of the retrieval where the signal in the 4.5–5.56 μm range alone would begin to saturate.

Despite these potential advantages, the retrieval from the broader 3.0–5.56 μm range may occasionally yield physically implausible outliers. For instance, in C3, a peak temperature of 430.9 K is reported under $\varepsilon_0 = 0.80$—a value well above what is expected for lunar surface conditions at that incidence angle. This suggests that residual artifacts or noise in the shortwave portion of the spectrum may corrupt the inversion under some conditions. These effects are not observed in the results from the 4.5–5.56 μm range, where temperature statistics behave smoothly and remain consistent with physical expectations.

Overall, these findings indicate that while the inclusion of wavelengths between 3.0 and 4.5 μm can, in principle, enhance retrievals in low-radiance scenes by increasing the spectral baseline, this benefit is offset by increased sensitivity to calibration uncertainties and reflectance modelling. In high-SNR, thermally bright observations such as C3 and C4, the narrower 4.5–5.56 μm range appears to offer more stable and physically reliable results. It minimizes sensitivity to the crossover region and avoids the numerical dominance of channels with mixed solar and thermal contributions.

These considerations support a context-dependent approach to spectral selection: the full 3.0–5.56 μm range may prove useful in cold or poorly illuminated scenes, whereas the more conservative 4.5–5.56 μm window is preferable when strong thermal emission is present. Future improvements in the treatment of solar reflectance and absolute calibration in the shortwave infrared may enable more confident use of the full range, but under current processing conditions, restricting the inversion to wavelengths dominated by thermal emission yields more robust and interpretable results.

A final test was performed by applying a Lommel–Seeliger photometric correction to the MAJIS spectra in the range 3.0–5.56 μm before retrieval, with the aim of reducing possible biases linked to viewing and illumination geometry. The Lommel–Seeliger law, originally formulated in the late 19th century to describe single scattering from dark planetary surfaces (Lommel, 1887; Seeliger, 1888), has long been applied to lunar observations as a simple and effective photometric correction. Its role was later formalized within the more general radiative transfer framework of Hapke (1981), where it is recognized as a limiting case particularly suited to the Moon's porous regolith under moderate illumination conditions. The Lommel–Seeliger correction was implemented pixel-by-pixel through the factor $\mu/(\mu+\mu_0)$, where $\mu = \cos(i)$ and $\mu_0 = \cos(e)$ being i and e the solar incidence and emission angle, respectively, and normalizing the observed radiance to a canonical geometry ($i = 60°$, $e = 30°$) reproducing the high phase angle (~90°) of the JUICE lunar flyby. However, it is precisely this extreme phase angle that makes the correction sub-optimal, which explains why the retrieved temperatures (Figure 6 and Table A3) are virtually indistinguishable from those obtained without photometric adjustment. This outcome indicates that, within the spectral interval used for retrieval and at the spatial resolution of MAJIS, photometric effects have little influence on the thermal inversion. The Moon's global shape can be approximated by a smooth ellipsoid at the few-hundred-meter pixel scale of MAJIS, so the primary driver of variability in the thermal signal is the distribution of insolation rather than geometric scattering. The Lommel–Seeliger law, while traditionally adopted for the diffuse scattering properties of the lunar regolith and effective at moderate phase angles where single scattering dominates, becomes less appropriate at the extreme phase angles encountered during the JUICE flyby. In this geometry, multiple scattering, surface roughness, and shadowing effects grow increasingly important, and a single-

parameter correction cannot capture such complexity. The absence of significant differences between corrected and uncorrected retrievals is therefore unsurprising and further supports the robustness of the Bayesian thermal inversion under the observing conditions of the JUICE flyby.

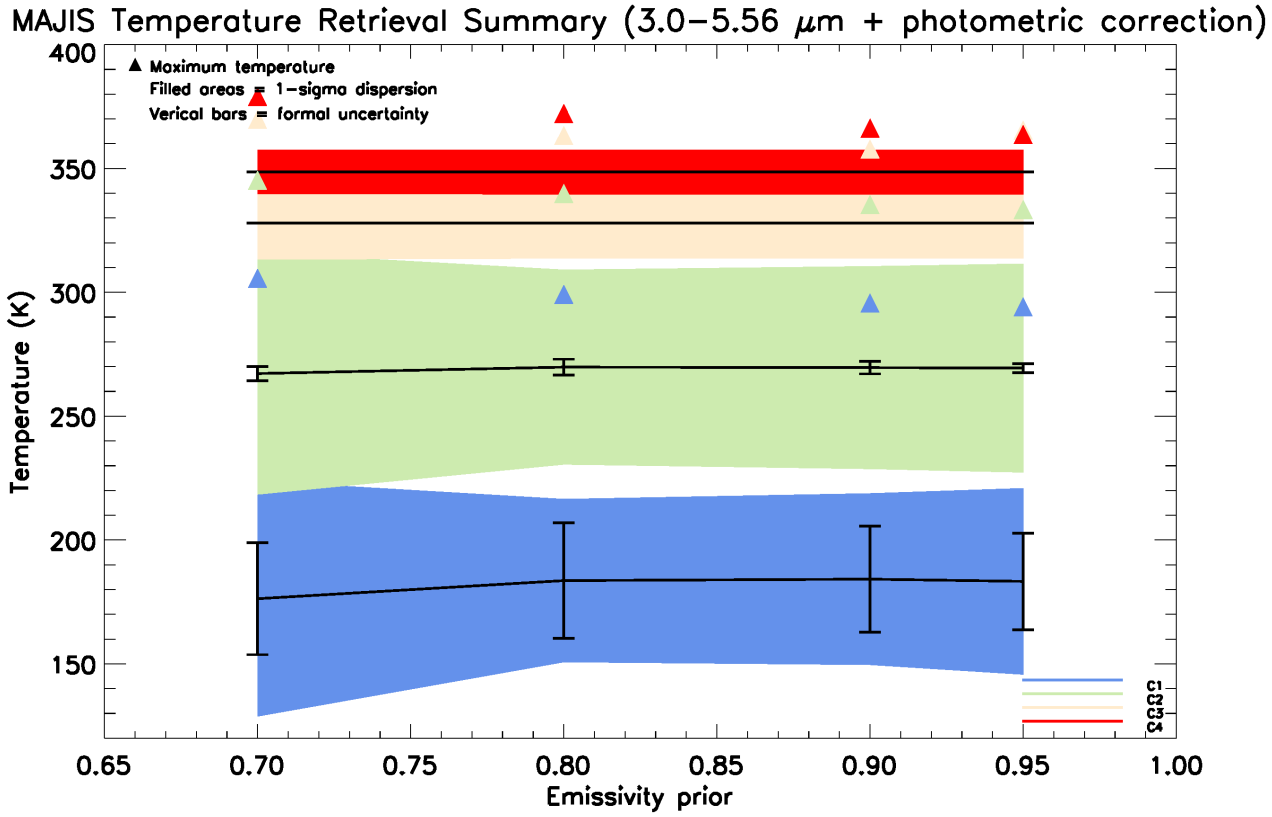

Figure 6. Summary of MAJIS temperature retrievals as a function of emissivity prior (3.0–5.56 µm range, Lommel–Seeliger correction applied). The coloured bands indicate the mean surface temperatures (solid lines) and associated ±1σ dispersion for the four MAJIS observations (C1–C4), derived from Bayesian inversion including the Lommel–Seeliger photometric correction. Vertical black bars show the mean formal uncertainties, and triangles mark the maximum retrieved temperature values. Compared to the uncorrected case, the photometric correction yields slightly smoother temperature trends and marginally reduced variability, especially across high incidence geometries.

For the subsequent intercomparison with the other methods (Section 2.5), we adopt the Bayesian retrieval parameters that provide the most physically plausible and stable results: the 4.5–5.56 µm spectral range, an emissivity prior of $\varepsilon_0 = 0.70 \pm 0.15$, and no photometric correction.

2.2 Empirical thermal correction

Li and Milliken (2016) developed an empirical thermal correction model tailored for spectra acquired by the Moon Mineralogy Mapper (M^3), which operated over the spectral range 0.43–3.0 μm (Pieters et al., 2009). They identified that at wavelengths beyond ~2 μm, thermal emission from the lunar surface contributes significantly to the measured radiance, particularly on the dayside. This thermal component can obscure or distort diagnostic absorption features associated with minerals and hydration, rendering accurate compositional analysis challenging.

To address this, they constructed a model grounded in laboratory measurements of lunar soils and glasses, leveraging the strong empirical correlation between reflectance at 1.55 μm (unaffected by thermal emission) and at 2.54 μm (where thermal emission may be substantial, depending on the surface temperature). This relationship follows a power law, enabling the prediction of the "true" reflectance at 2.54 μm based on the value at 1.55 μm. Any excess radiance at 2.54 μm is attributed to thermal emission, which can then be quantified and removed. Crucially, this approach allows for simultaneous estimation of the surface temperature, without requiring independent thermal measurements from instruments like Diviner, provided the observed materials match common lunar regolith compositions.

This method is particularly useful when applied to MAJIS data acquired in its visible and near-infrared (VISNIR) channel covering the spectral range 0.49–2.36 μm. While this does not extend as far into the thermal regime as M^3 (and the MAJIS-IR channel itself), thermal contributions can still become non-negligible near the upper end of this spectral window—especially for observations near local noon or in equatorial regions. Applying the Li and Milliken (2016) model to MAJIS data enables the detection and removal of this thermal component, improving the fidelity of the retrieved reflectance spectra. In doing so, it not only enhances mineralogical interpretations in the near-IR but also yields estimates of surface temperature derived directly from the observed radiance, assuming that a portion of the MAJIS spectrum captures the onset of thermal emission. This makes the approach particularly attractive for MAJIS lunar observations where Diviner-like thermal constraints may be unavailable or spatially mismatched, while allowing a direct comparison with the Bayesian method.

By grounding the correction in the inherent spectral behaviour of lunar soils and leveraging the statistical predictability of thermally unaffected wavelengths, this model provides a robust and computationally efficient tool for disentangling thermal and reflective components in hyperspectral datasets such as those from MAJIS.

Formally, the method proposed by Li and Milliken (2016) relies on two main equations. The first is Kirchhoff's law of radiative equilibrium:

$$I = 1/\pi \, F_{\mathrm{Sun}} \, R + I_{\mathrm{BB}}(T)(1-R) \qquad (2)$$

where I is the total radiance emitted by the surface, F_{Sun} the solar irradiance received by the surface, I_{BB} the blackbody radiance at temperature T associated with the surface thermal emission, and $R = 1-\varepsilon$ the surface reflectance, which is related to the emissivity ε under radiative equilibrium. The second equation is an empirical power-law relationship between the reflectances at 1.55 µm and 2.54 µm, measured in the laboratory on lunar soil and glass samples under the geometry $i = 30°$, $e = 0°$:

$$R_{2.54} = 1.124 \times R_{1.55}^{0.8793} \quad (3)$$

Assuming that thermal emission is negligible at 1.55 µm, i.e., $I_{1.55} \approx 1/\pi\ F_{Sun}\ R_{1.55}$, the thermal emission of the surface—and therefore its temperature—can be directly derived from the radiances measured by MAJIS at 1.55 and 2.54 µm, together with the incoming solar flux, without requiring additional assumptions about the surface emissivity. This makes the method computationally very efficient.

Nevertheless, over the range of lunar surface temperatures, the radiance excess at 2.54 µm can be small or even undetectable due to the radiometric uncertainty of MAJIS (see Langevin et al., this issue), which tends to scatter data points around the power-law curve (Figure 7). Consequently, all data points lying below the power-law relation correspond to surface temperatures that cannot be reliably estimated—or are highly uncertain—using this empirical approach. This limitation is most pronounced near the terminator (e.g., in C2), where thermal emission is weak and radiometric uncertainties dominate.

To assess the accuracy of the surface temperature estimates, in Figure 7 we compare our results with those predicted by the two-layer thermal equilibrium model proposed by Vasavada et al. (1999), with updated parameters based on LRO/Diviner observations (Vasavada et al., 2012). Our surface temperature estimates show good agreement with the model for solar incidence angles below 55° but diverge significantly at higher incidence angles. This discrepancy likely arises from unresolved sub-pixel topographic effects (e.g. mixed slopes and shadowing) that are not represented in the ellipsoid-based geometry and can locally bias the measured radiance. Sub-pixel slopes and shadowing can dominate the measured radiance and produce local deviations from the expected thermal behaviour. In the MAJIS observations, this incidence range corresponds to the highlands observed at the end of C3 and the beginning of C4. Part of the observed differences may also reflect the intrinsic mismatch between the MAJIS physical-temperature retrieval and the Diviner brightness-temperature products used for comparison. In terms of accuracy, assuming a 10% uncertainty in the radiometric flux measured by MAJIS, the corresponding uncertainties in surface temperature are estimated at ±15 K for C2, ±7 K for C3, and ±5 K for C4.

The Li and Milliken (2016) method also allows for an a posteriori determination of emissivity at 5.5 µm by inverting Kirchhoff's law, under the assumption that reflected sunlight at this wavelength is negligible, i.e., $I_{5.5} \approx \varepsilon_{5.5}\ I_{BB}(T)$. This capability will be further exploited in subsection 2.5.2, where emissivity retrievals obtained with different approaches are compared in detail.

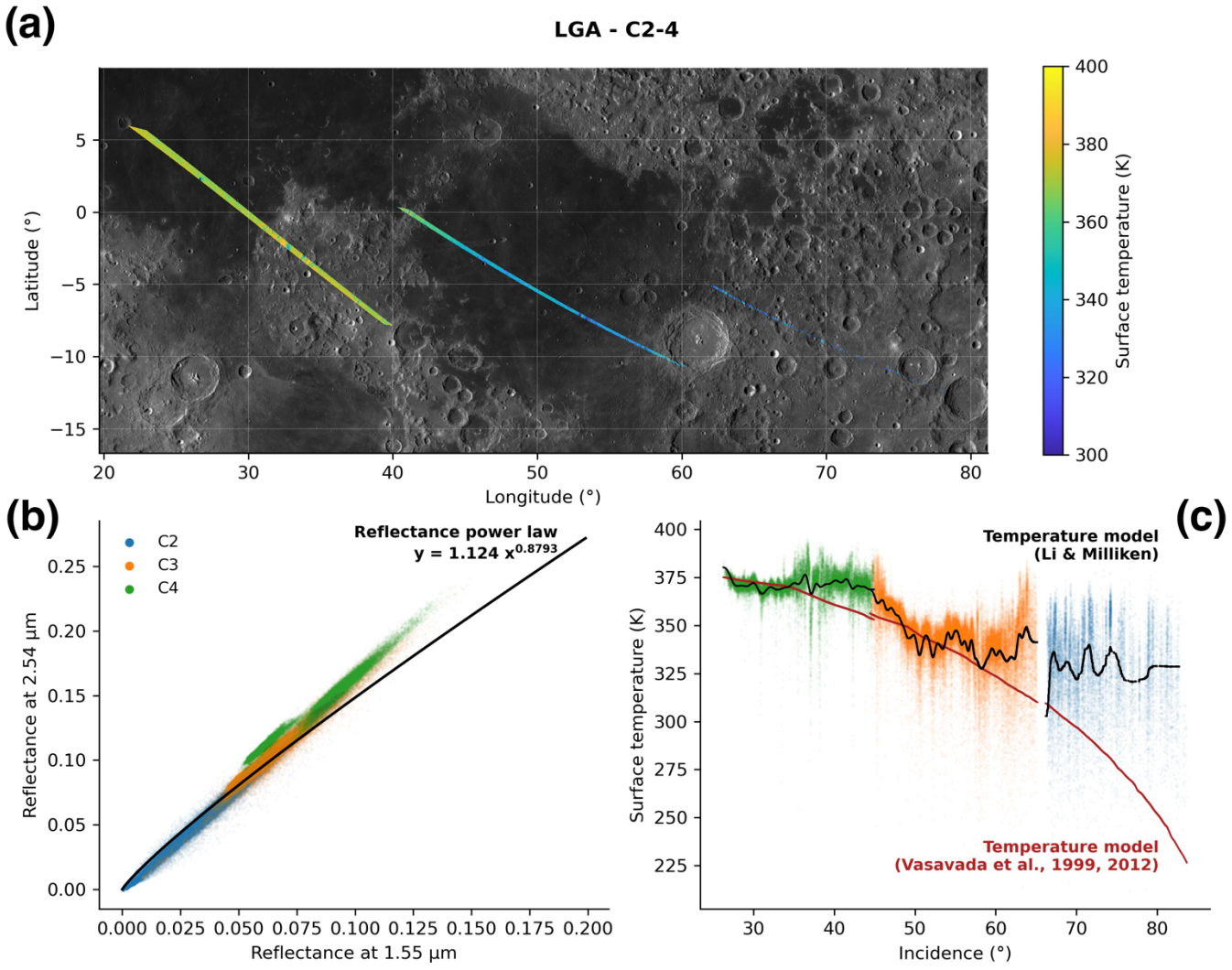

Figure 7. Empirical thermal correction results. Lunar surface temperature estimates on the MAJIS' C2–4 observations. (**a**): map of the temperature along MAJIS' tracks. Background image: Moon LRO LROC WAC Global Morphology Mosaic 100m, June 2013 (Speyerer et al., 2011; Wagner et al., 2015). (**b**): reflectance at 2.54 µm as a function of the reflectance at 1.55 µm illustrating the power law relation established by Li and Milliken (2016). Points above the black curve correspond to a "reflectance excess" due to thermal emission. (**c**): derived surface temperature and its median (black line) as a function of solar incidence. The red curve is the Vasavada et al. (1999, 2012) temperature model during the lunar day.

2.3 Roughness-informed thermal model

An additional approach builds upon the roughness-informed model introduced by Wohlfarth et al. (2023), originally developed to improve our understanding of the lunar diurnal water cycle based on M^3 observations. We adopt the treatment of both the

reflectance and thermal-emission components as described by Wohlfarth et al. (2023). In this framework, the reflectance contribution is modelled according to the Hapke formalism (Hapke, 2005), adopting the set of Hapke parameters reported by Li and Li (2011), whereas the thermal-emission component is implemented following the approach detailed in Wohlfarth et al. (2023). We note, however, that under the high phase-angle conditions of the JUICE lunar flyby (~90°), no photometric formulation can be regarded as strictly optimal, including Hapke-based corrections; in the present implementation, the Hapke term should therefore be viewed as a physically motivated approximation of the reflectance contribution rather than as a unique or fully constrained solution.

Unlike purely empirical approaches, the model represents sub-pixel roughness in terms of mm–cm scale RMS slope using synthetic fractal surfaces (Rozitis et al., 2020). These surfaces statistically reproduce unresolved topographic variability and allow the simulation of associated effects such as self-heating, sub-pixel shadowing, and multiple scattering. In this fractal representation, the surface is depicted as a series of discrete square plates, called "*facets*." The model solves the energy balance for each facet *m*, where the total flux F_m is the sum of three components: direct solar irradiation, scattered sunlight, and thermal self-heating from other facets. In our case, we divide each MAJIS pixel into a 65×65 sub-pixel grid, where the thermal balance is computed individually. The resolution of the sub-pixel facets provides a good compromise between capturing sub-pixel temperatures and computational tractability.

Once a sub-pixel synthetic fractal roughness surface is generated, the thermal contribution of the *m*-th facet is given by the energy balance equation:

$$F_m = F_m^{sun} + F_m^{sca} + F_m^{rad} \tag{4}$$

where F_m^{sun} is the flux of directly absorbed solar radiation, F_m^{sca} is the contribution of scattered sunlight from neighbouring sub-pixel facets and F_m^{rad} is the additional flux due to thermal self-heating. The thermal emission related to direct solar irradiation of the *m*-th sub-pixel facet is modelled as:

$$F_m^{sun} = (1 - A_{dh}) J_m \tag{5}$$

where A_{dh} is the directional–hemispherical albedo for the reflected sunlight (Shkuratov et al., 2011), here computed for each pixel following the workflow of Wöhler et al. (2017) and intrinsically connected to the single-scattering albedo, which is a free parameter of the model, while J_m is the incident solar irradiance on the *m*-th facet. The terms for scattering from neighbouring sub-pixel facets (F_m^{sca}) and thermal self-heating (F_m^{rad}) are respectively:

$$F_m^{sca} = (1 - A_{dh}) A_{dh} \sum_{j \neq m}^{65x65} f_{m,j} J_j + (1 - A_{dh}) {A_{dh}}^2 \sum_{j \neq m}^{65x65} f_{m,j} \sum_{k \neq j}^{65x65} f_{j,k} J_k + \ldots \tag{6}$$

$$F_m^{rad} = (1 - A_{dh,th}) \sum_{j \neq m}^{65x65} f_{m,j} F_j + (1 - A_{dh,th}) A_{dh,th} \sum_{j \neq m}^{65x65} f_{m,j} \sum_{k \neq j}^{65x65} f_{j,k} F_k + \ldots \quad (7)$$

where $f_{i,j}$ are the geometric view factors (Wohlfarth et al., 2023) and $A_{dh,th}$ is the directional–hemispherical albedo for self-heating (Wohlfarth et al., 2023), which is linked to the effective emissivity ε by Kirchhoff's law (Spencer, 1990). The reported equations are resolved in a matrix-vector notation to account for higher order terms for F_m^{sca} and F_m^{rad}, following the pipeline described by Wohlfarth et al. (2023). Subsequently, the Stefan–Boltzmann law relates the radiant flux of the *m*-th sub-pixel facet F_m to its equilibrium temperature, which can be retrieved jointly with the effective emissivity ε:

$$T_m = \left(\frac{F_m}{\varepsilon \sigma}\right)^{\frac{1}{4}} \quad (8)$$

Once the temperatures of the sub-pixel facets are estimated, the thermal emission component linked to the *n*-th pixel is defined as:

$$X_n(\lambda) = \frac{\sum_m^{65x65} P_m(\lambda) v_m cose_m}{\sum_m^{65x65} v_m cose_m} \quad (9)$$

where $P_m(\lambda)$ denotes the Planckian thermal emission of the *m*-th sub-pixel facet, computed from its estimated equilibrium temperature; v_m is a line-of-sight visibility factor to the sensor and e_m is the emission angle of the *m*-th facet.

The retrieval is performed in the 5.0–5.5 µm spectral range, which is dominated by thermal emission and largely unaffected by detector saturation. At this stage, single scattering albedo is optimized by minimizing the root mean square error (RMSE) between the modelled reflected radiance plus thermal emission $X_n(\lambda)$ and the observed MAJIS spectra.

The synthetic fractal surfaces are generated by using as free parameter the mm–cm scale roughness. However, applying a full coupled reflectance–thermal inversion based on synthetic fractal surfaces on a pixel-by-pixel basis over the entire hyperspectral cubes would be computationally demanding and, more importantly, not warranted by the information content of all datasets. We therefore retrieve representative average mm–cm scale roughness values only for selected regions of interest (ROIs), chosen to sample the main terrain units.

In particular, we use the C4 radiance dataset for the mm–cm scale roughness retrieval because this hyperspectral cube provides the most favorable illumination geometry and the strongest thermal contribution. As a result, the modeled radiance exhibits the highest sensitivity to mm–cm scale roughness. In contrast, for cubes C1 and C2 the thermal signal is comparatively weak and the measured radiance is largely dominated by noise, which prevents a robust constraint on surface roughness and introduces a strong degeneracy with the single-scattering albedo. For this reason, retrieving mm–cm scale roughness independently for C1 and C2 would lead to poorly constrained solutions with limited physical interpretability. Instead, we adopt the terrain-representative mm–cm scale roughness values derived from the C4 cube for the analysis of the other datasets.

Nevertheless, degeneracies intrinsic to thermophysical models may still affect the retrieval even for C4. To assess and mitigate this effect, we performed 20 independent simulations for each ROI, varying the initial guesses for both roughness and single-scattering albedo. These simulations generally converge to slightly different solutions without any evident outlier, which can be used to estimate the uncertainties of the retrieved parameters and to evaluate the impact of model degeneracy. Within this framework, the mm–cm scale roughness is found to be well constrained, whereas the single-scattering albedo shows a maximum variability of about 20% within both ROIs.

The ROIs selected to constrain the mm–cm scale roughness and single-scattering albedo at 5.5 µm in the C4 hyperspectral cube are listed in Table 2. The retrieved mm–cm scale roughness values are then compared with meter-scale roughness estimates derived from the LOLA Digital Roughness Map (LRO/LOLA LDRM_32 data; Smith et al., 2010, 2017). Both quantities are expressed as terrain RMS slope: the spatial distribution of the LOLA-derived meter-scale roughness is shown in Figure 8, while the ROI-averaged values are reported in Table 2.

Table 2. Terrain type, geographic coordinates, retrieved sub-pixel roughness, and single-scattering albedo for the specific ROIs defined to derive average values of sub-pixel-scale roughness.

Terrain type / hyperspectral cube	**Geographical context of the ROI**	**Average mm–cm roughness (θ_{RMS})**	**Average meter-scale roughness LRO/LOLA (θ_{RMS})**	**Single-scattering albedo ($\omega_{5.5\mu m}$)**
Mare-like / C4	3.5 – 5.0°N 23.7 – 25.1°E	(20.64° ± 0.91°)	(3.31° ± 0.88°)	(0.55 ± 0.10)
Highland-like / C4	3.0 – 4.3°S 32.5 –35.5°E	(26.97° ± 2.66°)	(9.88° ± 3.40°)	(0.59 ± 0.10)

We assume that the average mm–cm scale roughness values reported in Table 2 are representative of the corresponding terrain units (mare-like and highland-like) across the C1–C4 hyperspectral cubes. These roughness values are expected to be comparable within the JUICE/MAJIS footprints, consistent with the behaviour observed across the lunar surface, as indicated by previous studies (e.g., Wohlfarth et al., 2023). With this approach, we account for realistic mm–cm scale average roughness values across different terrain types while avoiding a full pixel-by-pixel retrieval, which would be computationally expensive and strongly affected by parameter degeneracy in low-SNR hyperspectral cubes, as for C1 and C2. Results indicate that the average mm–cm scale roughness values are overall higher in terms of RMS slope than those inferred at the meter scale.

This outcome is broadly consistent with results from previous studies, which generally report roughness values of ~20°–35° depending on observation geometry and retrieval approach. Near-nadir observations typically yield mm–cm scale roughness estimates of ~20°–25° (e.g. Bandfield et al., 2015; Wohlfarth et al., 2023), whereas more oblique configurations commonly give higher values, generally around ~30°–35° (e.g. Rubanenko et al., 2020; Müller et al., 2021). The values retrieved in this

study (Table 2) fall within the lower-to-intermediate part of this range. This is noteworthy because the roughness retrieval is based on C4, whose emission angles (Table 1) correspond to distinctly off-nadir viewing geometry rather than a near-nadir configuration. The comparatively moderate values obtained here may therefore reflect differences in instrument characteristics, phase angle (~90°), spectral range, and modelling assumptions relative to previous studies. In addition, effective incidence angles are computed by combining the observing geometry with local terrain slopes from LOLA Digital Slope Map (LRO/LDSM_16 data) (Smith et al., 2010, 2017), thereby better reproducing the actual physical illumination conditions (Figure 9).

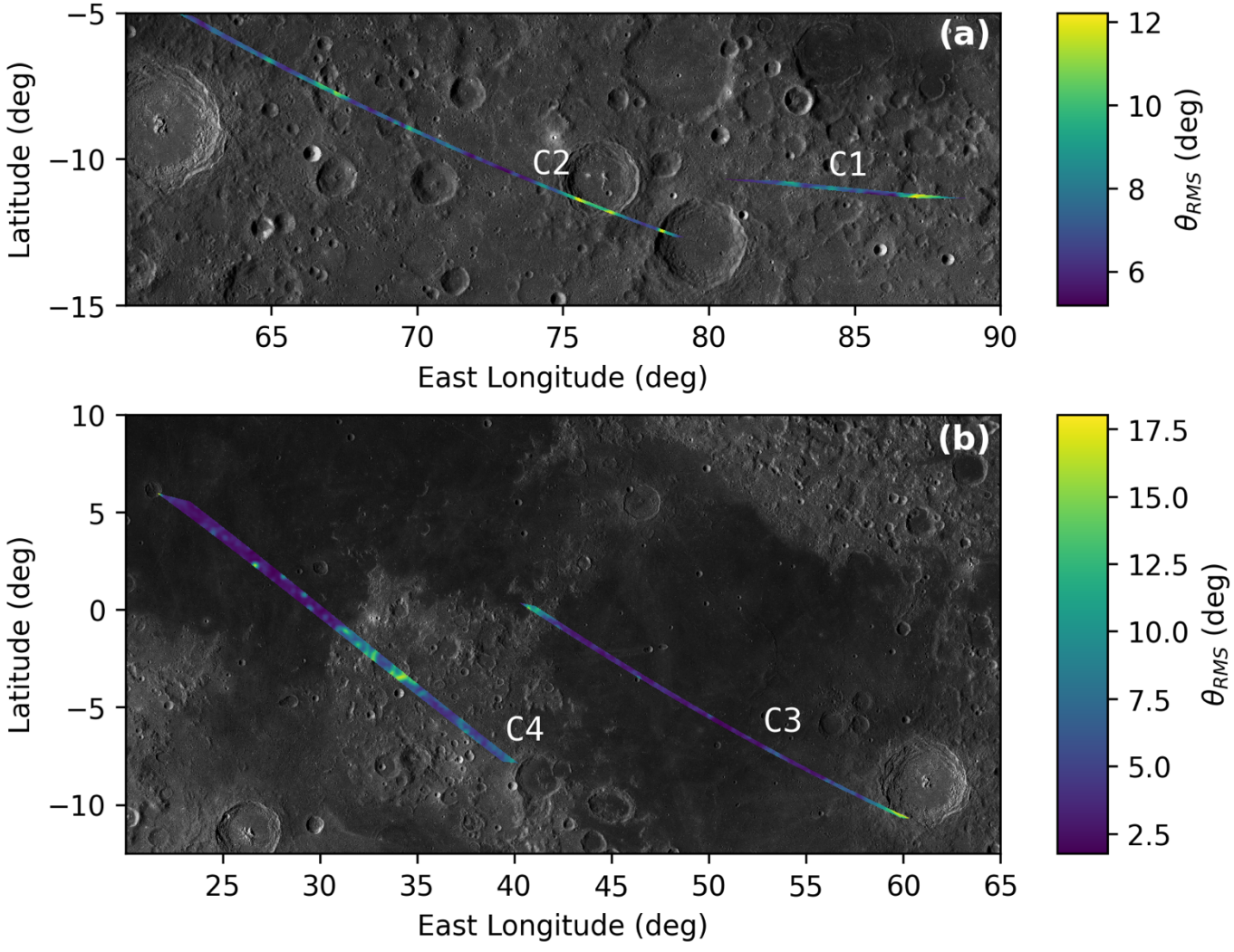

Figure 8. LOLA-derived meter-scale roughness maps. Estimated meter-scale roughness (RMS slope) derived from LDRM_32 LRO/LOLA data, interpolated with a Gaussian filter to match the spatial resolution of the four MAJIS observations: (**a**) C1 and C2; (**b**) C3

and C4. Background image: Moon LRO LROC WAC Global Morphology Mosaic 100m, June 2013 (Speyerer et al., 2011; Wagner et al., 2015).

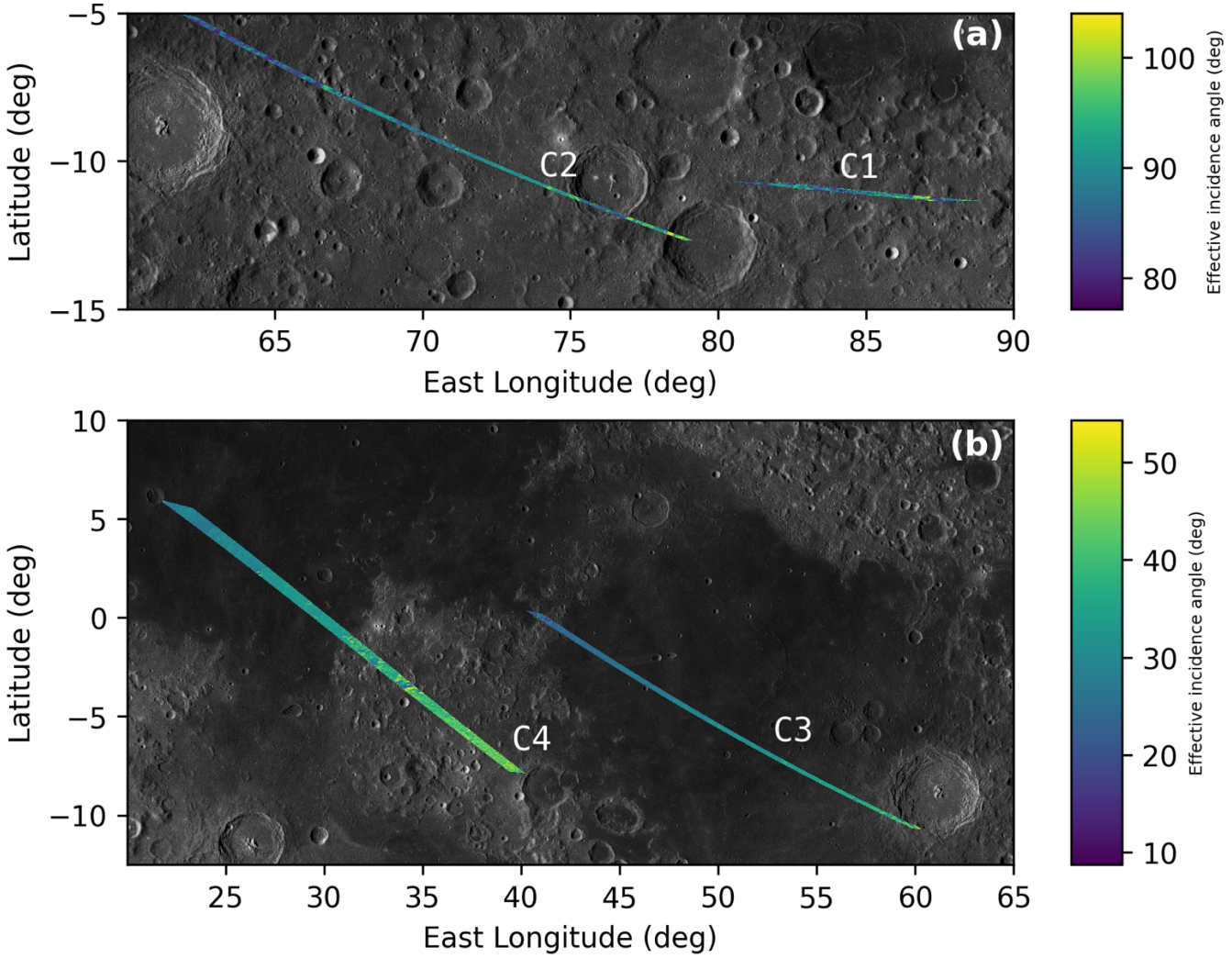

Figure 9. Effective solar incidence angles. Effective incidence angles derived combining the observational geometries with the local terrain slopes from LDSM_16 LRO/LOLA data, convolved to match the spatial resolution of the MAJIS observations: (**a**) C1 and C2; (**b**) C3 and C4. The variability associated with local topography is most evident in C1 and C2, where the altimetric variations measured by LRO/LOLA significantly alter solar incidence across rugged terrains. Background image: Moon LRO LROC WAC Global Morphology Mosaic 100m, June 2013 (Speyerer et al., 2011; Wagner et al., 2015).

After constraining the mm–cm scale roughness in specific ROIs (Table 2), temperatures retrieved from each MAJIS hyperspectral cube are reported in Figure 10. The retrieved temperatures exhibit a clear spatial correlation with the effective

illumination conditions (Figure 9). The highest temperature value (383 K) is observed in the northwestern sector of C4, consistent with the local incidence angles and in agreement with the location of maximum temperature identified by the other two methods. Furthermore, low-albedo terrains exhibit higher surface temperatures than brighter terrains at the same local solar time. This behaviour is evident in the transition region between Mare Tranquillitatis and the adjacent highland-like terrain in C4 (Figure 10). Conversely, the lowest temperature values (<150 K) occur in shadowed regions of C1 and C2, corresponding to pixels characterized by effective incidence angles exceeding 90° (Figure 10).

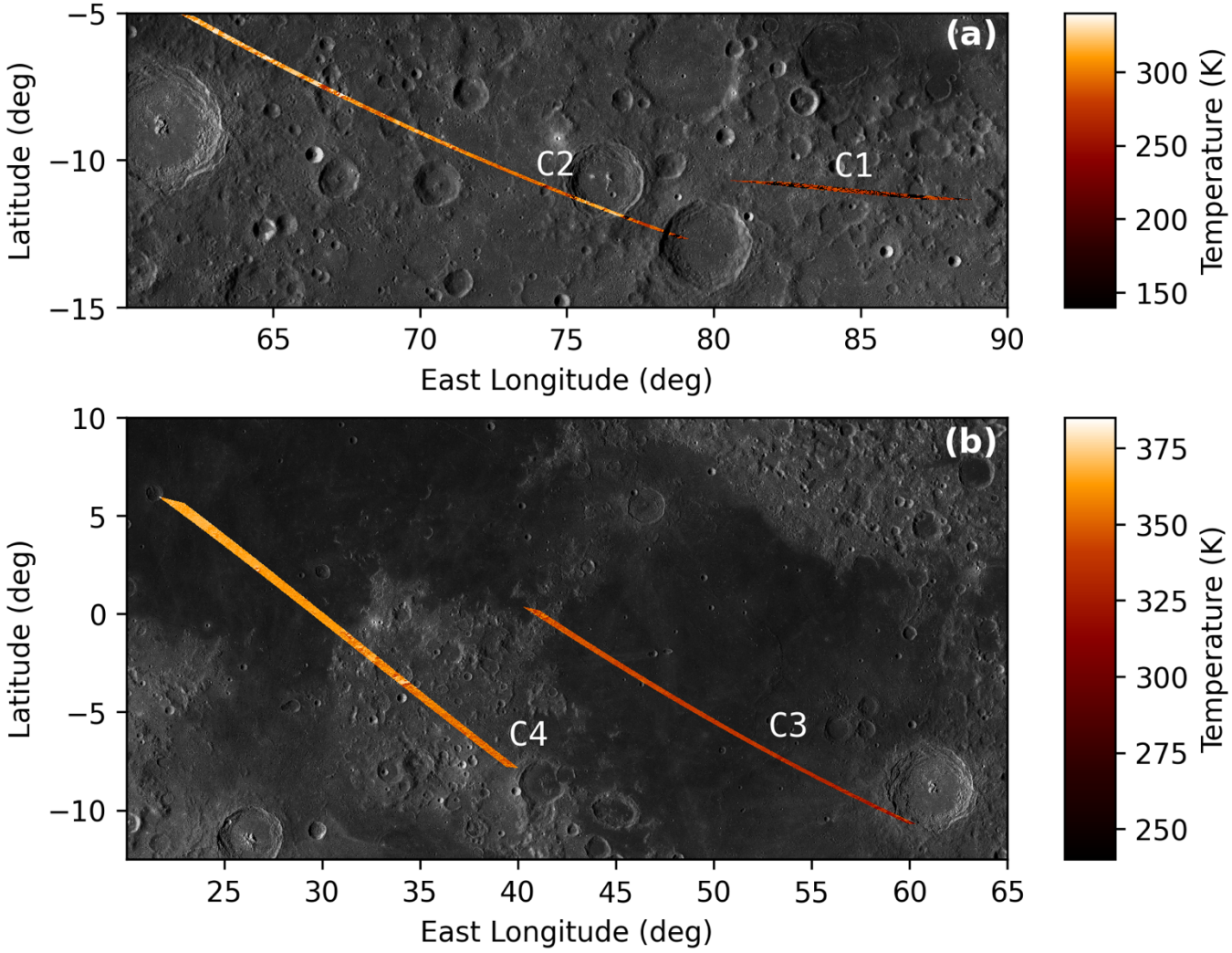

Figure 10. Temperatures from roughness-informed model. Temperatures retrieved using the roughness-informed thermal model: (**a**) C1 and C2; (**b**) C3 and C4. Spatial variations in the temperatures are primarily controlled by effective illumination conditions (Figure 9) and sub-pixel mm–cm scale roughness (Table 2). The maximum temperature value (383 K) is observed in the northwestern portion of C4, whereas the lowest values (<150 K) occur in C1 and C2, within areas strongly affected by local topographic shading, corresponding to non-

illuminated surfaces ($i > 90°$), as highlighted in Figure 9. Background image: Moon LRO LROC WAC Global Morphology Mosaic 100m, June 2013 (Speyerer et al., 2011; Wagner et al., 2015).

To further assess the influence of roughness assumptions, we perform a similar analysis by assuming the mm–cm scale roughness to be equal to the meter-scale roughness measured by LRO/LOLA (Figure 8). This test is intended to evaluate the similarities and differences in the resulting temperature estimates.

In our case, the sub-pixel roughness at the mm–cm scale is significantly higher than the meter-scale roughness (Table 2), which may lead to different contributions from self-heating, self-shadowing, and scattered sunlight. A direct comparison between the temperatures retrieved under the two assumptions for C3 and C4 is shown in Figure 11.

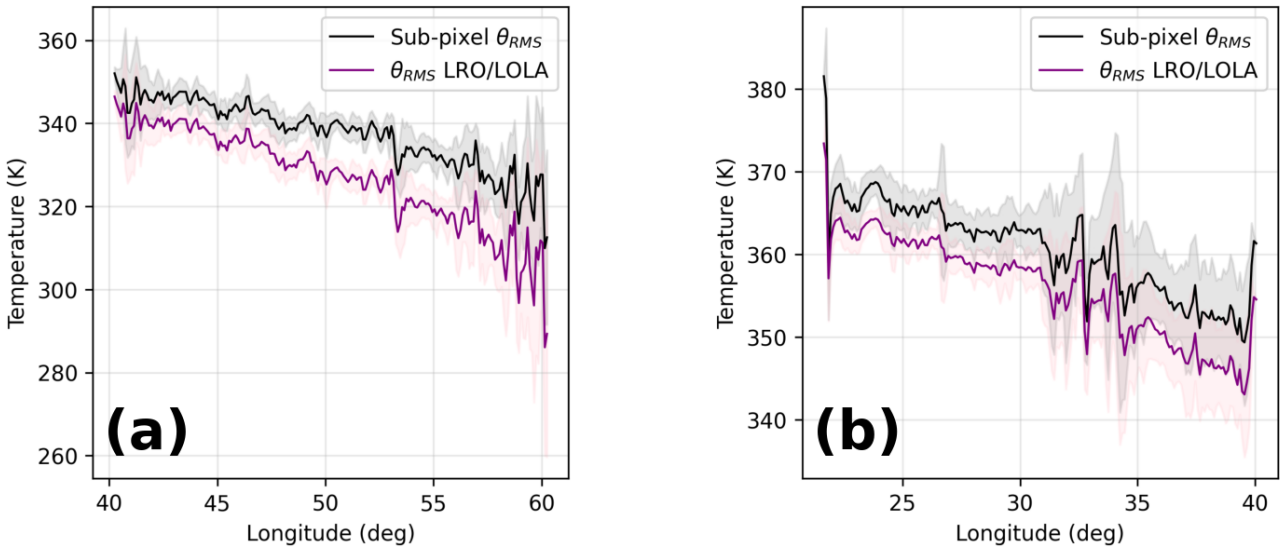

Figure 11. Effect of roughness on retrieved surface temperatures (C3–C4). Surface temperature variations computed using the average mm–cm scale roughness value (black line) and the meter-scale roughness values derived from LRO/LOLA data (purple line) for the sub-pixel fractal surface generation, shown for C3 (a) and C4 (b). The shaded areas correspond to the 1–σ dispersion after binning with a longitudinal step of 0.1°.

The results shown in Figure 11 highlight the differences between a full thermophysical inversion, in which the average sub-pixel roughness is retrieved, and the assumption that mm–cm scale roughness matches the meter-scale roughness derived from LRO/LOLA measurements (Figure 9). Within the longitude range between 22.5° and 46.0°, the retrieved temperatures are partially comparable within the associated uncertainties—defined as the 1–σ dispersion after binning the data with a longitudinal step of 0.1°—although temperatures derived using the mm–cm scale roughness are on average slightly higher.

This result suggests that self-heating, self-shadowing, and scattering effects are mitigated—and therefore less sensitive to surface roughness—at low incidence angles, as expected from previous studies (Spencer, 1990; Wohlfarth et al., 2023).

Beyond 46° longitude, the two approaches begin to diverge (Figure 11), with temperature differences exceeding the associated uncertainties and therefore no longer comparable within the 1–σ error bars. In particular, the skin temperature retrieved using the mm–cm scale roughness values derived from the thermophysical modelling (Table 2) is systematically higher than that obtained when the meter-scale roughness derived from LRO/LOLA is adopted instead. This behaviour indicates that the terms dominating Eq. 4 become increasingly sensitive to micro-scale slopes at higher incidence angles. Higher roughness values correspond to steeper slopes at the mm–cm scale, which enhance the radiative interaction between facets and increase the contribution of the self-heating term, as expected (Spencer, 1990). The largest variation is observed for C3 at longitude of 56.2°, corresponding to a temperature difference of (15.3 K ± 11.8 K). The spatial distribution of the temperature differences between the two assumptions is reported in Figure A2.

2.4 Cross-wavelength comparison with LRO/Diviner

To place the MAJIS thermal observations into a broader lunar context, we compared our results with co-located datasets from the Diviner Lunar Radiometer Experiment aboard LRO (Williams et al., 2017). Diviner provides radiance and brightness temperature for channels 3–6 (7.8–25 μm), along with derived emissivity maps and the Christiansen Feature (CF) wavelength. For this work, we gathered Diviner radiances for channels 3–6 acquired under sub-solar longitudes between –26° and +18°. Following Williams et al. (2018), the field of view of each measurement was modelled using a Monte-Carlo distribution of 50 points to compute its effective footprint.

Radiances were then adjusted to the solar distance corresponding to the JUICE flyby (1.014 au) under the assumption of radiative equilibrium, and subsequently gridded at 128 pixels per degree. Because Diviner does not provide full spatial coverage at the exact solar geometry of the MAJIS observations (sub-solar longitude -4.1°, sub-solar latitude 1.0°), we estimated gap-free radiances by linearly interpolating the observations bracketing each pixel in sub-solar longitude. This procedure reproduces the large-scale thermal structure well, though orbit-to-orbit striping remains visible in places (Figure 12). CF position and peak brightness temperature were determined by parabolic fitting of channels 3, 4 and 5 (Greenhagen et al., 2010), and channel emissivities were evaluated relative to the CF peak temperature. We note that Diviner products provide brightness-temperature quantities (including the peak brightness temperature around the CF) rather than a direct estimate of physical thermodynamic surface temperature. In this work, the Diviner peak brightness temperature is used as a practical proxy for the surface thermal state, since it is derived near the CF where the effective emissivity is expected to be close to unity and the dependence on emissivity is reduced compared to single-channel brightness temperatures. This approach highlights compositional and textural contrasts between mare and highlands, although emissivity estimates at large incidence angles (i > 60°) are strongly affected by photometric roughness effects, particularly in channel 6.

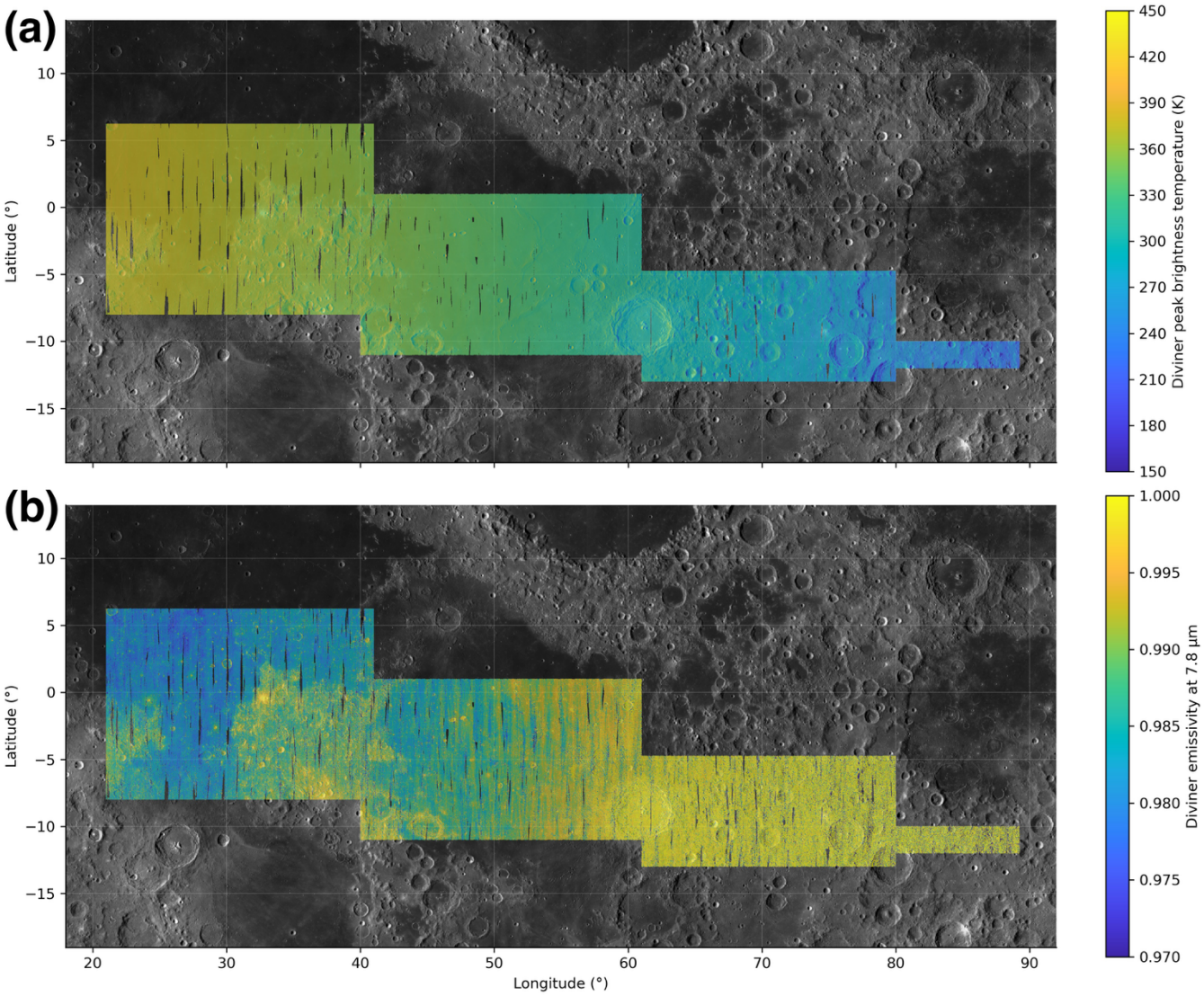

Figure 12. Diviner brightness temperature and emissivity. (**a**) Diviner peak brightness temperature (channels 3–6, 7.8–25 µm) over the MAJIS ground track, gridded at 128 px/degree (~240 m/px at the equator) and interpolated across adjacent sub-solar longitudes to match the illumination of the JUICE flyby. The map captures the large-scale thermal contrast between Mare Tranquillitatis and the surrounding highlands, with minor orbit-to-orbit striping. (**b**) Emissivity at 7.8 µm (Diviner channel 3), computed relative to the Christiansen Feature using the standard CF-fitting procedure. This wavelength is sensitive to compositional and textural differences. Background image: Moon LRO LROC WAC Global Morphology Mosaic 100m, June 2013 (Speyerer et al., 2011; Wagner et al., 2015).

2.5 Comparison of the three methods

2.5.1 Temperature

The comparison between three independent approaches for estimating lunar surface temperature from MAJIS data reveals systematic differences that depend on solar incidence angle and the radiometric quality of the observations. Figure 13 summarizes the results of (1) Bayesian inversion (Tosi et al., 2014), (2) an empirical correction based on laboratory-derived relationships (Li and Milliken, 2016), and (3) a roughness-informed thermal model (Wohlfarth et al., 2023).

The comparison among the three retrieval approaches highlights systematic differences that depend strongly on solar incidence angle and illumination conditions. The empirical correction following Li and Milliken (2016) increasingly diverges from the Vasavada thermal model at incidence angles beyond ~55°. This behaviour likely reflects the fact that the correction law was derived from laboratory spectra acquired under fixed geometry (i = 30°, e = 0°), conditions that differ markedly from the high phase angle (~90°) and variable incidence sampled during the JUICE flyby. By contrast, the Bayesian inversion shows greater robustness at high incidence and low-SNR data, producing smoother and more conservative temperature estimates that remain relatively close to the Vasavada curve. However, a notable deviation between Methods 1 and 2 and the Vasavada model is observed in the longitude range 30–40° corresponding to highland terrains observed in C4 under incidence angles in the range 35°–45°, where surface roughness and anisothermality introduce systematic biases. The roughness-informed Model 3 (Wohlfarth et al., 2023) can reproduce the expected temperature trends under well-illuminated conditions (i < 60°), but in the present implementation its agreement with Diviner and with the Vasavada model is not systematically better than the other approaches and depends on the adoption of the Hapke's model for the reflected component. In fact, this approach may lead to deviations in the derived single-scattering albedo because the photometric treatment becomes more uncertain at phase angle ~90°. This potential discrepancy may partially propagate into the roughness values retrieved in Section 2.3, which depend directly on the single-scattering albedo, and consequently into the retrieved temperatures. Nonetheless, in shadowed or high incidence regions, even this approach remains challenged by anisothermality and unresolved sub-pixel topography, which introduce localized deviations.

Taken together, these results are an intercomparison of the specific implementations used here, rather than evidence of intrinsic complementarity among the methods. The empirical correction performs best when the observing geometry is close to its laboratory calibration conditions, but it becomes increasingly sensitive to extrapolation at high phase angle and high incidence. The Bayesian inversion is comparatively stable in low-SNR regimes in this study, largely due to the strength of the a priori regularization, which can also damp local variability at intermediate incidence angles. The roughness-informed approach can reduce geometry-driven biases by explicitly representing sub-pixel facet distributions in the forward model; however, its performance in this work is strongly implementation-dependent (e.g., roughness scaling and photometric/albedo parameterization), and therefore it should be interpreted as a physically motivated sensitivity test rather than a uniformly superior solution.

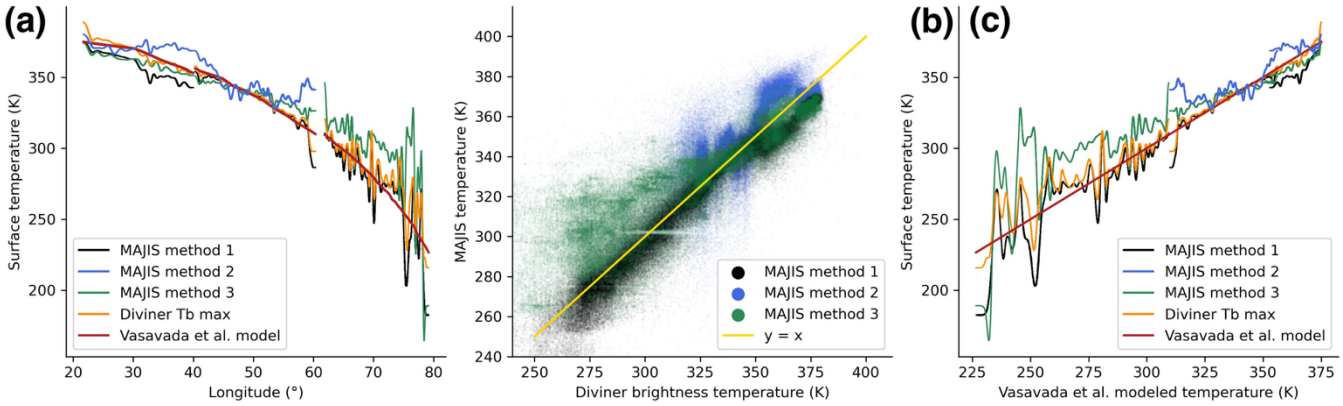

Figure 13. Comparison of temperature retrieval methods. Surface temperature estimates from MAJIS infrared data obtained with three independent approaches: (1) Bayesian inversion following Tosi et al. (2014) (black), (2) empirical correction following Li and Milliken (2016) (blue), and (3) a roughness-informed thermal model following Wohlfarth et al. (2023) (green). (**a**): retrieved temperatures along the JUICE ground track as a function of longitude, compared with Diviner maximum brightness temperatures (orange) and the thermophysical model of Vasavada et al. (1999) (red). (**b**): pixel-by-pixel comparison between MAJIS-derived temperatures and Diviner brightness temperatures, with the one-to-one line in yellow. (**c**): comparison between MAJIS- and Diviner-derived temperatures, and the Vasavada et al. (1999) model. All methods converge within a few kelvins under well illuminated conditions, though larger deviations occur near the terminator.

2.5.2 Emissivity

Before comparing emissivity results, we clarify that different retrieval approaches naturally return different emissivity quantities. In Method 1 (Bayesian inversion), emissivity is retrieved as a spectral, channel-by-channel directional emissivity over the thermal window (4.5–5.56 µm), and for map-level comparison we report the value at 5.5 µm. In Method 2 (empirical correction), emissivity at 5.5 µm is inferred from the measured radiance using the approximation $I_{5.5} \approx \varepsilon_{5.5} B_\lambda(T)$, assuming that the reflected component is negligible at this wavelength for the considered scenes; the resulting should thus be interpreted as an effective emissivity tied to the adopted temperature estimate and viewing geometry. In Method 3 (roughness-informed model), emissivity is treated as spectrally neutral over 5.0–5.5 µm and retrieved jointly with temperature within a sub-pixel facet formulation; the retrieved parameter represents a grey effective emissivity that absorbs residual directional and sub-pixel effects not explicitly captured by the simplified spectral emissivity assumption. In this section, the intercomparison is therefore restricted to a common observable: an effective directional emissivity at 5.5 µm under the MAJIS observation geometry.

With this definition, Figure 14 compares emissivity estimates from the MAJIS lunar observation C4 that are consistent in wavelength (5.5 µm) and in observational meaning (effective directional emissivity), while differences among methods

primarily reflect their distinct modelling assumptions and implementation choices; the comparison is shown both in map view and as longitudinal profiles.

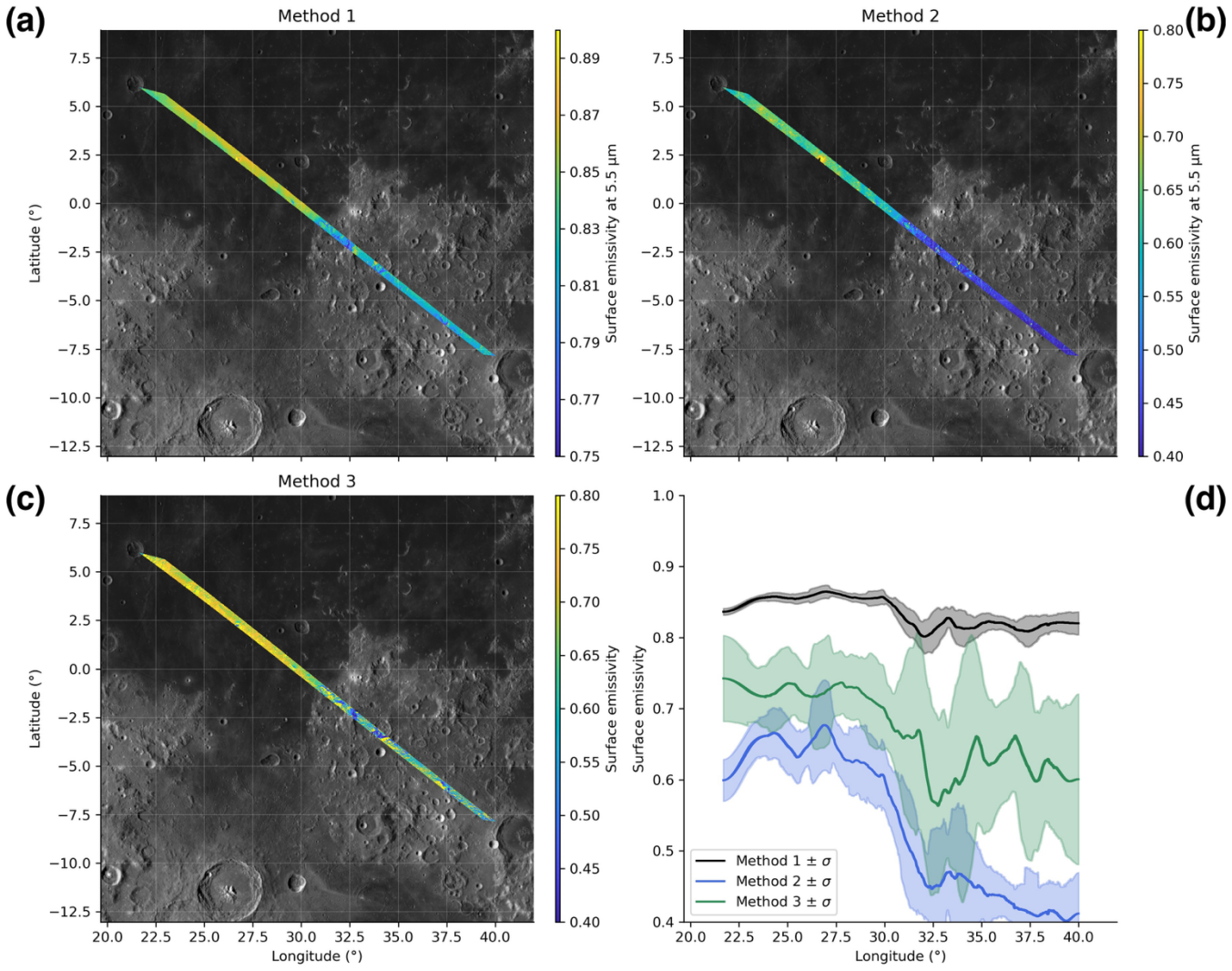

Figure 14. Comparison of emissivity retrieval methods. Emissivity estimates for the C4 observation obtained with the Bayesian approach or Method 1 (**a**), the Li and Milliken method or Method 2 (**b**), and the roughness-informed thermal model or Method 3 (**c**), respectively. Background image: Moon LRO LROC WAC Global Morphology Mosaic 100m, June 2013 (Speyerer et al., 2011; Wagner et al., 2015). Panel (**d**) shows a comparison between the emissivity estimated with Method 1 (black shaded plot), Method 2 (blue shaded plot) and Method 3 (green shaded plot) as a function of longitude.

Figures 14a–c present the spatial distribution of emissivity at 5.5 μm derived with the Bayesian inversion (Method 1), the empirical correction (Method 2), and the roughness-informed thermal model (Method 3), respectively. In Method 1, full spectral emissivity profiles between 4.5 and 5.5 μm are retrieved using a prior of 0.70 ± 0.15, and only the scalar value at 5.5 μm is mapped. Method 2 computes emissivity at the same wavelength directly from Kirchhoff's law, assuming negligible reflected sunlight, whereas Method 3 retrieves emissivity over 5.0–5.5 μm by explicitly including roughness and illumination geometry in the forward radiative transfer. Panel 14d summarizes these results as a function of longitude, allowing direct comparison of terrain-dependent variability among the three approaches.

All methods detect the same first-order geophysical signal: Mare Tranquillitatis exhibits higher emissivity than the surrounding highlands. However, the magnitude and variability of emissivity differ substantially across methods. The Bayesian inversion (black shaded plot in Figure 14d) yields values tightly clustered around $\varepsilon \approx 0.85$ in the mare and 0.75–0.85 in the highlands with minimal scatter, reflecting the smoothness constraint imposed by the prior covariance. The empirical method (blue shaded plot) produces significantly lower values (0.60–0.70 in the mare and 0.40–0.60 in the highlands) and shows enhanced pixel-to-pixel noise. Method 3 (green shaded plot) returns similar values—$\varepsilon \approx 0.60$–0.70 in the mare and $\varepsilon \approx 0.50$–0.80 in the highlands—with greater variability in rough or cratered areas. This variability is consistent with the inherently directional nature of emissivity and the influence of surface slopes on thermal emission (e.g., Rozitis and Green, 2011).

Although Methods 2 and 3 both assume spectrally neutral emissivity over their retrieval interval, their behaviour in highland regions differs markedly. Method 3 systematically yields higher emissivity than Method 2, falling between the Bayesian and empirical estimates. This indicates that the underestimation by Method 2 is not solely due to the grey-emissivity assumption, but also to its neglect of roughness (and associated beaming effects), its reliance on laboratory calibration relationships obtained at fixed geometry, and the propagation of uncertainties from the multiple wavelengths used in the correction. By explicitly accounting for geometry and roughness, Method 3 mitigates several of these limitations, even within a narrower spectral range.

The spatial maps further illustrate these differences in retrieval fidelity. The Bayesian-derived map (Figure 14a) shows a smooth and coherent emissivity pattern that closely reflects the large-scale thermophysical contrast between mare and highlands. The empirical map (Figure 14b) displays stronger noise and variability, particularly over highland terrains, while the roughness-informed model (Figure 14c) preserves the large-scale trend and captures localized fluctuations in rough areas and along crater rims, consistent with its explicit sensitivity to surface geometry. Despite their methodological differences, all three approaches reproduce the same first-order emissivity dichotomy between mare and highlands.

This contrast aligns with known compositional and textural differences. Feldspathic highland regoliths are more porous and finely comminuted, enhancing multiple scattering and lowering effective emissivity, whereas denser, smoother basaltic mare surfaces exhibit higher emissivity (e.g., Donaldson Hanna et al., 2012). This interpretation is consistent with full-disk observations from NOAA/HIRS (3.75–15 μm) analysed by Müller et al. (2021), who reported systematically lower emissivity over highlands—particularly beyond 5 μm—and attributed this to variations in composition, grain size, and roughness. Additional context in the 3–4 μm domain is provided by disk-resolved mid-infrared observations from the geostationary

Gaofen-4 (GF-4) satellite. Wu et al. (2021) imaged the full lunar disk in the MIR band 6 (3.50–4.10 μm; effective wavelength ~3.77–3.82 μm depending on the relative reflected/thermal contribution). Their analysis highlights that, at these wavelengths, the measured radiance is governed by the interplay of reflected sunlight and thermal emission, and that maria can appear brighter than highlands under warm conditions due to enhanced thermal emission from low-albedo basalts. While GF-4 does not provide hyperspectral emissivity retrievals, it independently confirms that the 3–5 μm region is a crossover regime in which temperature–emissivity coupling and illumination geometry strongly affect inferred surface properties.

Complementary context at longer wavelengths is provided by Lucy/L'TES, which acquired hyperspectral thermal-infrared lunar spectra in the range 5.8–100 μm during the 2022 Earth gravity assist and derived emissivity spectra consistent with Diviner Christiansen-feature constraints and Apollo soil laboratory measurements (Christensen et al., 2025). This TIR benchmark anchors the interpretation of the Diviner comparison below, emphasizing that mare–highland emissivity ordering depends on wavelength and bandpass across the CF-related spectral structure.

When compared with Diviner, a clear bandpass dependence emerges. The Diviner emissivity product discussed here is derived for channel 3 (7.8 μm), i.e. on the short-wavelength side of the Christiansen Feature (CF) for feldspathic highland materials (e.g., Greenhagen et al., 2010). Because mare basalts typically exhibit CF positions at longer wavelengths than feldspathic terrains, the emissivity measured in Diviner channel 3 can therefore be higher over highlands than over maria at this specific wavelength (see Figure 11b in Ren et al., 2021), even though the relative ordering may differ at shorter wavelengths. Accordingly, the Diviner channel-3 comparison should be interpreted as a narrow-band diagnostic linked to CF position and composition, rather than as evidence that highlands are generally more emissive than maria across the mid-infrared.

In the MAJIS range (≤5.56 μm), our emissivity estimates indicate higher values over mare basalts than over surrounding highlands, consistent with independent measurements in the 3–5 μm region (e.g., Chandrayaan-2/IIRS; Ojha et al., 2024) and with published laboratory spectra showing that emissivity contrasts can vary with wavelength and composition. The comparison with Diviner thus provides complementary context across wavelength regimes: MAJIS samples the short-wavelength side of the CF and the crossover region between reflected and emitted radiance, whereas Diviner channel 3 samples the CF flank near 7.8 μm. This combined view highlights the need to interpret emissivity in terms of wavelength-dependent, bandpass-specific quantities rather than a single "bulk" emissivity, especially when comparing instruments that sample different parts of the CF-related spectral structure.

The CF positions derived from Diviner additionally provide an independent compositional indicator that complements MAJIS hyperspectral retrievals at shorter wavelengths, reinforcing the distinction between mare basalts and feldspathic highlands. In practice, Diviner offers long-wavelength, global coverage with excellent diurnal sampling, while MAJIS provides high-resolution hyperspectral measurements in the 3.0–5.56 μm range, bridging the gap between near- and mid-infrared observations. Taken as a whole, these datasets support the wavelength-dependent nature of lunar emissivity and the importance of multi-instrument analyses for disentangling the combined effects of composition, texture, roughness and thermal environment on airless-body surfaces.

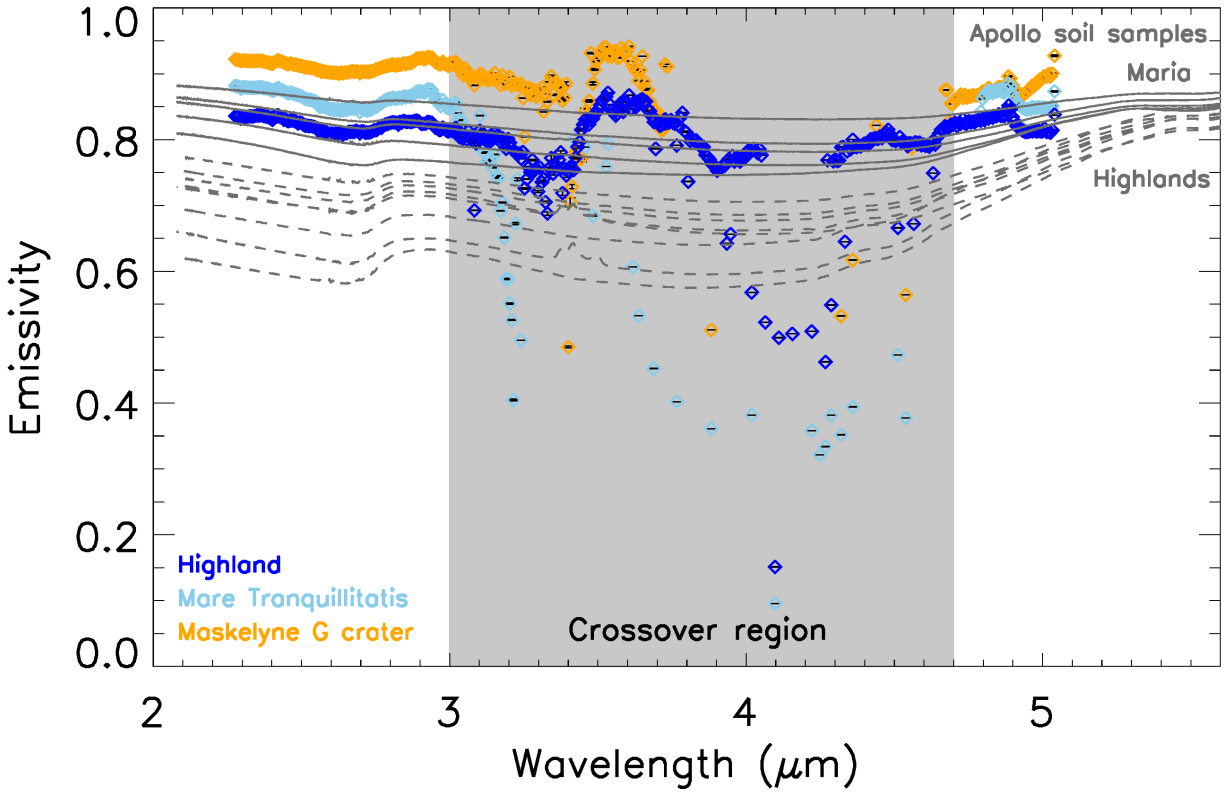

765

Figure 15. Spectral emissivity of different terrains. Spectral emissivity profiles for three lunar surface units retrieved with the Bayesian inversion applied to MAJIS C4 data. The thermal retrieval is performed over the 3.0–5.56 μm interval, and the resulting emissivity is reported here as spectral directional emissivity under the opaque-surface assumption. For wavelengths shorter than 3.0 μm, emissivity is extended using the photometrically corrected reflectance via Kirchhoff's relation $\varepsilon_d(\lambda)=1-r_{hd}(\lambda)$. Shown are terrain-averaged emissivity profiles for a
770 highland region (blue), Mare Tranquillitatis (cyan), and the Maskelyne G crater (orange). For qualitative laboratory context, emissivity spectra of Apollo soil samples are overplotted in grey, with representative mare and highland sample groups indicated with solid and dashed lines, respectively. Formal uncertainties on the MAJIS emissivity averages are very small and are shown as black markers. The shaded region marks the 3.0–4.7 μm crossover interval, where reflected and emitted contributions are comparable and emissivity retrievals are most sensitive to modelling assumptions and residual calibration effects.

775

Building on this result, Figure 15 presents representative spectral emissivity profiles extracted from three distinct lunar terrains: highlands, Mare Tranquillitatis, and Maskelyne G, a 6-km fresh crater located within the mare. These profiles reveal clear, systematic differences that reflect underlying variations in composition and surface texture. The spectra were derived using the Bayesian inversion method applied to MAJIS data in the 3.0–5.5 μm range, under the assumption of an emissivity prior of
780 0.70 ± 0.15 and no photometric correction. Across the spectral interval, the highland spectrum shows the lowest emissivity

values, typically between 0.78 and 0.85, consistent with the known properties of feldspathic materials. Mare Tranquillitatis exhibits higher emissivity across the same wavelengths, indicative of denser, basaltic composition and surface texture differences. The Maskelyne G crater spectrum displays the highest emissivity, close to or above 0.90 throughout the thermal domain, consistent with exposure of coarser, less-weathered or blocky material exhibiting reduced multiple scattering and enhanced thermal emission (Salisbury et al., 1987; Mustard and Hays, 1997; Donaldson Hanna et al., 2012), and potentially enhanced by localized self-heating and thermal-infrared beaming within concave or rough crater interiors (Rozitis and Green, 2011; Davidsson and Rickman, 2014). Mineralogical analysis of the same MAJIS dataset indicates that this crater is compositionally distinct from the surrounding terrain, showing an enhanced abundance of pyroxene-rich material, possibly pigeonite (Zambon et al., this issue).

While the emissivity differences between terrains are geologically meaningful, the presence of apparent absorption-like minima—particularly between 3.0 and 4.7 µm—requires careful interpretation. These features are not associated with known silicate vibrational bands, which typically occur beyond 8 µm, outside the MAJIS spectral range. Instead, they likely result from challenges in retrieving emissivity in the transition region where reflected solar and thermally emitted radiation overlap. In this "crossover region," small errors in radiometric calibration, assumed surface reflectance, or modelling of solar contribution can propagate into the retrieval, leading to artificial depressions in emissivity. To assess whether the ~3.5 µm structure reflects a systematic signal in the input measurements, we inspected the C4 data in radiance space, excluding the first 17 slit samples that were intentionally omitted from the thermal analysis because of the straylight test configuration. No scene-wide absorption centred at ~3.5 µm is found in the median radiance spectrum. The corresponding channel shows only modest sample-dependent residuals, generally within a few percent across the usable slit region. We therefore do not regard the ~3.5 µm structure as a robust scene-wide spectral feature in the radiance data; rather, any corresponding depression seen in retrieved emissivity should be interpreted in the context of the reflected/thermal separation in the crossover regime. For additional context, in Figure 15 we also compared the MAJIS spectral profiles of retrieved emissivity with laboratory emissivity spectra (calculated as 1 - reflectance) of Apollo soil samples available in the ECOSTRESS database (https://speclib.jpl.nasa.gov/library). The comparison should be interpreted qualitatively, because the MAJIS retrieval yields an effective directional emissivity under the JUICE flyby geometry, whereas the Apollo spectra represent laboratory emissivity measured under controlled conditions. Within the MAJIS retrieval window (3.0–5.56 µm), Figure 15 primarily demonstrates a reproducible relative offset among the terrain-averaged emissivity curves extracted from the selected highland, mare, and fresh-crater regions. In the thermally dominated part of the spectrum, mare basalts and Maskelyne G exhibit systematically higher retrieved emissivity than the surrounding highlands, consistent with the first-order mare–highland contrast observed in the emissivity maps (Figure 14) and with the expected wavelength dependence of lunar emissivity. A weak qualitative similarity can be noted in the 2.5–2.8 µm range, where the MAJIS-derived emissivity profiles display a relative variation broadly comparable to that observed in the Apollo soil spectra. On the other hand, the 3.0–4.7 µm crossover interval is ill-conditioned for reflected/thermal separation, so the relative ordering of terrain-averaged emissivities near ~4 µm may be

affected by retrieval/calibration residuals; we therefore emphasize the thermally dominated part of the MAJIS window for geophysical interpretation.

3 Conclusions

The MAJIS observations obtained during the JUICE lunar flyby provide an appealing opportunity to assess the thermal and emissivity properties of the Moon at high spatial and spectral resolution. By applying three independent approaches—Bayesian inversion (Tosi et al., 2014), empirical correction following Li and Milliken (2016), and a roughness-informed thermal model following Wohlfarth et al. (2023)—we derived surface temperatures and emissivity values that can be cross-validated against one another and compared with both Diviner datasets and thermophysical models. These methodological differences are also relevant for reflectance-based analyses around 3 μm, where residual thermal emission can bias inferred band strengths.

Although this study does not perform a dedicated lunar hydration analysis, the thermal-removal problem addressed here is directly relevant to the interpretation of possible absorptions around 3 μm. Companion work by Langevin et al. (this issue) reports a weak, broad structure near ~2.9 μm in MAJIS radiance spectra acquired at mid-to-high incidence, but explicitly cautions that its interpretation is limited because this spectral interval coincides with the LVF–interface spectral gap—also discussed by Zambon et al. (this issue)—and because reflectance band-strength estimates in this region are highly sensitive to the model-dependent subtraction of the thermal contribution in the reflected/thermal crossover regime.

The comparison among methods highlights both convergence and divergence. All three techniques reproduce the expected temperature increase with solar illumination, with agreement within a few kelvins in the most favourable radiometric conditions (C3–C4). However, their behaviour diverges at higher incidence angles or in low-SNR scenes. The empirical approach, being tied to laboratory-derived correction laws, tends to overestimate surface temperatures under geometries far from its calibration range, particularly at $i > 55°$, where the relative contribution of reflected radiance increases and the temperature–emissivity separation becomes more degenerate. The Bayesian approach, by contrast, remains more stable under these conditions but shows a tendency to underestimate peak temperatures at intermediate incidence angles, a likely manifestation of over-regularization. The roughness-informed thermal model can reduce geometry-driven biases by representing sub-pixel facet distributions in the forward model, but its agreement with Diviner/Vasavada in this study remains implementation-dependent and varies across scenes (e.g., assumptions on roughness scaling, albedo).

A central result of this study is the characterization of bandpass-specific emissivity contrasts across major lunar terrains within the MAJIS thermal range (≤5.56 μm). Despite methodological differences, the three approaches consistently retrieve higher effective emissivity over Mare Tranquillitatis than over the surrounding feldspathic highlands, with locally enhanced values over fresh crater interiors such as Maskelyne G. This contrast is consistent with established compositional and textural differences between basaltic and feldspathic units (e.g., varying mafic mineral content and space-weathering state), and with geometry-dependent effects linked to surface roughness. While micro-texture (including porosity and packing state) may contribute to effective emissivity, the present daytime flyby data do not provide independent constraints on thermal inertia or

thermal conductivity; we therefore restrict the interpretation to emissivity contrasts inferred in the MAJIS bandpass under the observed geometries. This interpretation is also supported by the terrain-averaged spectral emissivity profiles of Figure 15, which show a reproducible relative offset among the selected highland, mare, and fresh-crater units within the MAJIS spectral range. In particular, the thermally dominated part of the spectrum consistently shows higher retrieved emissivity for mare basalts and Maskelyne G than for the surrounding highlands, whereas the 3.0–4.7 μm crossover interval remains more sensitive to reflected/thermal separation and should not be over-interpreted in terms of diagnostic absorption features.

The comparison with Diviner is used here to provide cross-wavelength context rather than a direct emissivity equivalence. Diviner channel-3 emissivity at 7.8 μm samples the short-wavelength flank of the Christiansen Feature for feldspathic materials; because mare CF positions occur at longer wavelengths, highlands can appear more emissive than maria at this specific wavelength. This behaviour is therefore interpreted as a narrow-band effect controlled by CF position and composition, not as evidence that highlands are generally more emissive than maria across the mid-infrared. In combination, MAJIS (≤5.56 μm) and Diviner (7.8 μm) emphasize that emissivity must be interpreted as a wavelength-dependent, bandpass-specific quantity when comparing instruments sampling different parts of the CF-related spectral structure.

Independent measurements in adjacent mid-infrared regimes further support the need for a bandpass-specific interpretation of lunar radiance and emissivity. Gaofen-4 acquired disk-resolved images of the Moon in a 3.50–4.10 μm band (effective wavelength ~3.8 μm), showing that the mid-infrared lunar appearance is governed by the combined contribution of reflected sunlight and thermal emission, with maria becoming brighter than highlands under conditions where thermal emission dominates and with the brightness distribution evolving with illumination geometry (Wu et al., 2021). At longer wavelengths, Lucy/L'TES provided well-calibrated hyperspectral thermal-infrared (TIR) lunar spectra and retrieved an emissivity spectrum with a Christiansen-feature maximum near 8.15 μm that agrees with Diviner CF constraints and Apollo soil laboratory spectra (Christensen et al., 2025). Together, these complementary datasets emphasize that apparent mare–highland emissivity ordering can change with wavelength across the CF-related spectral structure, and that cross-instrument comparisons must be framed in terms of the specific bandpasses and observation geometries involved.

The roughness-informed thermal model adds an important dimension by explicitly accounting for sub-pixel temperature variability (i.e., mixtures of sunlit and shadowed facets with different slopes within one pixel). This helps interpret deviations observed at high incidence angles and over rugged terrains, where unresolved slopes and shadowing can bias temperature retrievals based on simplified radiative balance assumptions. In the present implementations, the empirical method is most sensitive to these effects because it assumes a fixed-geometry correction law, whereas the Bayesian approach may damp such variability through regularization. By incorporating roughness-driven facet distributions within an energy-balance framework, the roughness-informed model mitigates some of these biases, although localized deviations remain in the most extreme geometries and/or lowest-SNR conditions.

The thermophysical patterns retrieved by MAJIS show a clear correspondence with the mineralogical variability independently identified in the VNIR domain (Zambon et al., this issue). In Mare Tranquillitatis, areas exhibiting deep 1–2 μm pyroxene absorptions—indicative of Fe- and Ca-rich basalts—tend to coincide with higher effective emissivity and warmer daytime

temperatures, consistent with compositional differences (mafic vs feldspathic units) and with variations in surface maturity. In contrast, feldspathic highlands, spectrally dominated by plagioclase and characterized by strong space-weathering reddening, show lower emissivity and more heterogeneous thermal behaviour. Local thermal enhancements near fresh craters similarly match VNIR detections of compositionally fresher, blocky pyroxene-rich materials. These correlations indicate that the 3–5.5 μm radiance field and the corresponding effective emissivity products are modulated by composition and surface maturity, in addition to illumination geometry and unresolved roughness.

Taken together, the MAJIS observations demonstrate that, under favourable conditions, the retrieval framework yields well-constrained formal uncertainties and reproduces the main daytime thermal patterns and bandpass-specific emissivity contrasts at MAJIS resolution, while additional systematic limitations remain in the crossover interval where reflected and emitted components are comparable. The combined analysis indicates that variations in composition, surface maturity, and unresolved roughness/illumination geometry jointly modulate the retrieved temperature and effective emissivity fields, while limitations remain in the crossover interval where reflected and emitted components are comparable.

These results help define the observational conditions under which MAJIS mid-infrared radiances can be interpreted most reliably over well-characterised lunar terrains, and they highlight the regimes in which model assumptions have the strongest influence on the solution. In this sense, the lunar dataset serves as a physically constrained test case for thermal retrievals in the mid-infrared crossover region. While instrument-level validation is addressed elsewhere, the present analysis shows that physically motivated inversion schemes can reproduce the main thermal behaviour of the observed lunar scenes without conflict with established lunar constraints. Although the thermophysical properties of the Galilean satellites differ from those of the Moon, the retrieval strategy developed here provides a methodological basis for future applications to MAJIS observations of icy surfaces, including cases where thermal emission may become detectable near the long-wavelength edge of the instrument range (Royer et al., 2025).

Appendix A

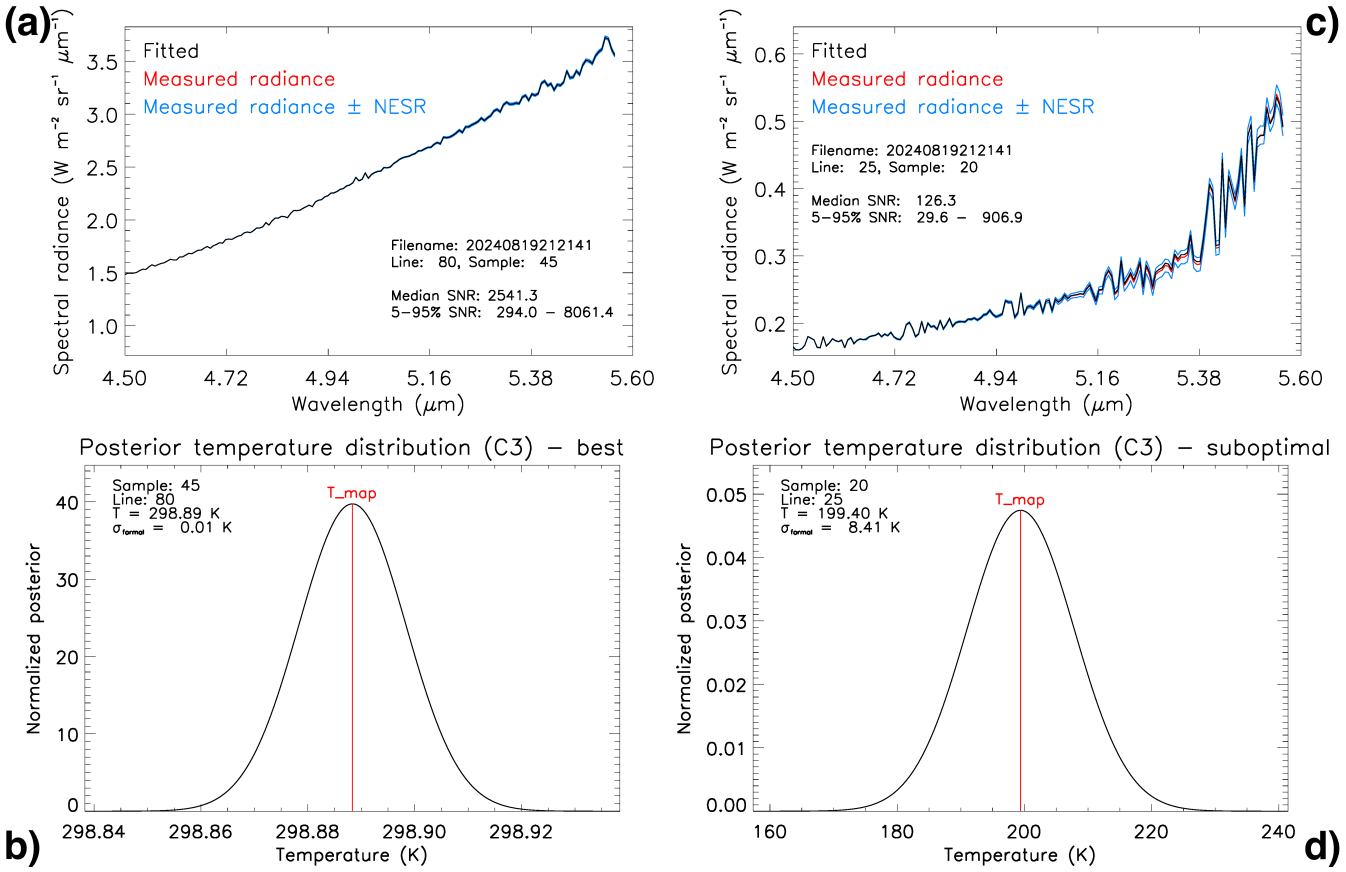

Figure A1. Example MAJIS thermal retrievals and associated posterior temperature distributions for observation C3. (**a**) Radiance fit for a best-case pixel (sample = 45, line = 80) from the MAJIS C3 observation (file 20240819212141), retrieved over 4.5–5.5 µm assuming an initial emissivity prior $\varepsilon_0 = 0.7$. The measured radiance spectrum (red) is closely reproduced by the model fit (black). The blue curves show the measured radiance ± NESR, plotted on the same axis to illustrate the relative noise level across the retrieval interval. For this pixel, the median SNR over 4.5–5.5 µm is ~2541, with a 5–95 % SNR range of ~294–8061. (**b**) Corresponding posterior probability density of surface temperature, approximated as a Gaussian centred at the maximum-a-posteriori estimate T_{map} (red vertical line), with width given by the formal 1-σ uncertainty from the posterior covariance matrix. (**c**) Same as in panel (**a**), but for a suboptimal pixel (sample = 20, line = 25), characterized by lower radiance levels and larger relative noise. For this pixel, the median SNR over 4.5–5.5 µm is ~126, with a 5–95 % SNR range of ~30–907. (**d**) Corresponding posterior temperature distribution for the suboptimal pixel, showing a broader distribution consistent with the larger formal uncertainty.

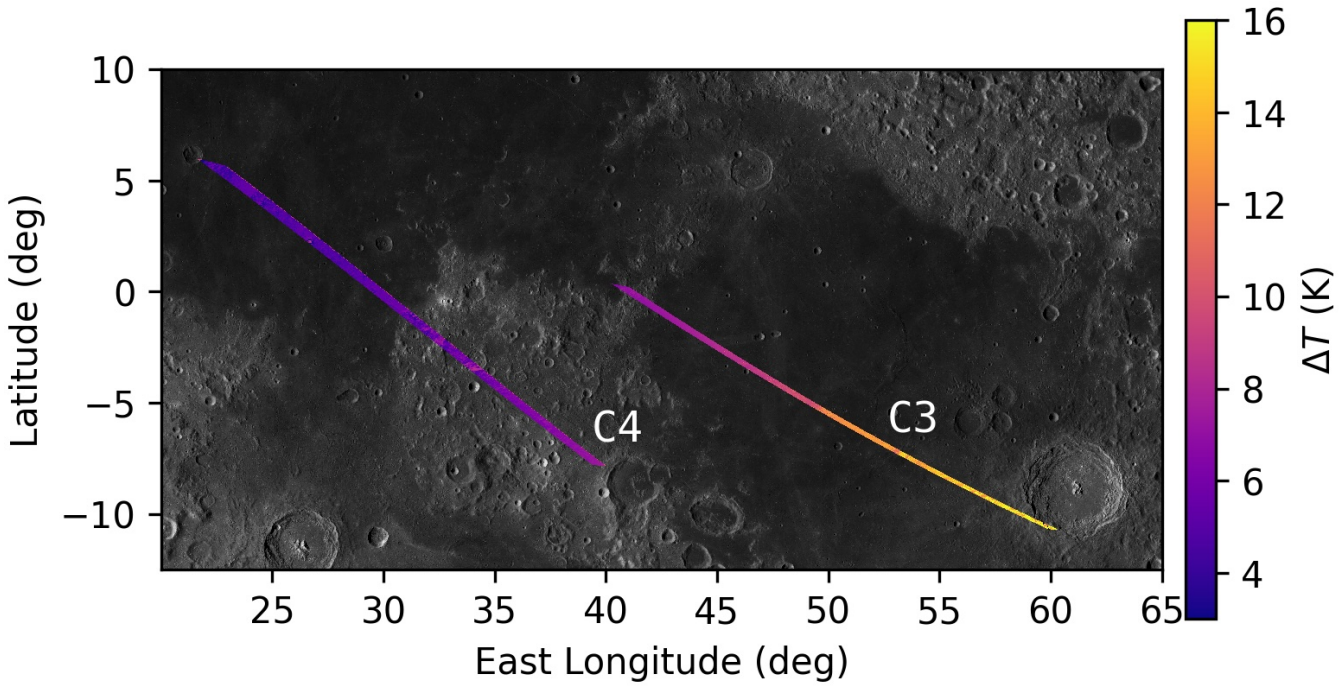

Figure A2. Temperature sensitivity to sub-pixel roughness assumptions (C3–C4). Temperature differences obtained when assuming sub-pixel roughness values retrieved in Table 2 compared with the assumption that the meter-scale roughness derived from LRO/LOLA measurements at meter scale represents the sub-pixel roughness. Differences remain small (mostly <5 K) for C4, consistent with the favourable illumination conditions. For C3, the temperature difference increases with increasing longitude and solar incidence angle (Figure 11), in agreement with previous studies (e.g., Bandfield et al., 2015; Wohlfarth et al., 2023).

Table A1. Summary of the temperature values obtained by applying the Bayesian approach to the four data acquired by MAJIS, using the 4.5–5.56 µm range and applying no photometric correction. The different columns specify the a priori hypotheses on the initial emissivity (ε_0) along with maximum associated standard deviation. For each MAJIS data, the following information is reported: mean temperature value, mean formal uncertainty associated with the data, 1-sigma dispersion of the data, and maximum temperature value. Units are kelvin.

Observation	**Parameter**	$\varepsilon_0 = 0.7 \pm 0.15$	$\varepsilon_0 = 0.8 \pm 0.20$	$\varepsilon_0 = 0.9 \pm 0.10$	$\varepsilon_0 = 0.95 \pm 0.05$
C1	T_mean	175.7	184.0	184.3	183.3
	σ_formal	22.5	23.1	21.3	19.5
	σ_data	48.5	32.5	34.6	37.6
	T_max	305.6	299.1	295.6	294.1
C2	T_mean	267.8	270.0	269.4	269.2
	σ_formal	3.0	3.2	2.5	1.8
	σ_data	49.0	39.2	40.8	41.7
	T_max	345.2	339.9	335.4	333.4

C3	T_mean	333.4	329.2	325.7	324.2
	σ_formal	0.8	0.4	0.4	0.2
	σ_data	16.1	14.6	13.4	12.8
	T_max	369.8	363.3	357.8	365.4
C4	T_mean	355.9	350.1	345.2	343.0
	σ_formal	1.4	1.5	0.7	0.3
	σ_data	9.6	9.1	8.7	8.5
	T_max	379.0	372.1	366.3	363.7

Table A2. Summary of the temperature values obtained by applying the Bayesian approach to the four data acquired by MAJIS, using the 3.0–5.56 µm range and applying no photometric correction. The different columns specify the a priori hypotheses on the initial emissivity (ε_0) along with maximum associated standard deviation. For each MAJIS data, the following information is reported: mean temperature value, mean formal uncertainty associated with the data, 1-sigma dispersion of the data, and maximum temperature value. Units are kelvin.

Observation	**Parameter**	$\varepsilon_0 = 0.7 \pm 0.15$	$\varepsilon_0 = 0.8 \pm 0.20$	$\varepsilon_0 = 0.9 \pm 0.10$	$\varepsilon_0 = 0.95 \pm 0.05$
C1	T_mean	176.3	183.6	180.2	183.3
	σ_formal	22.6	23.3	19.6	19.5
	σ_data	47.5	32.9	39.7	37.6
	T_max	301.6	298.5	293.6	294.2
C2	T_mean	267.2	269.8	269.6	269.4
	σ_formal	2.9	3.2	2.5	1.8
	σ_data	48.8	39.3	40.9	42.1
	T_max	340.1	405.2	340.1	340.1
C3	T_mean	328.0	328.0	328.0	328.0
	σ_formal	0.0	0.0	0.0	0.0
	σ_data	14.7	14.3	14.2	14.2
	T_max	362.3	430.9	365.6	365.7
C4	T_mean	348.6	348.6	348.6	348.6
	σ_formal	0.0	0.0	0.0	0.0
	σ_data	8.9	9.0	9.0	9.0
	T_max	383.1	399.3	382.0	378.8

Table A3. Summary of the temperature values obtained by applying the Bayesian approach to the four data acquired by MAJIS, using the 3.0–5.56 µm range and applying the Lommel–Seeliger photometric correction. The different columns specify the a priori hypotheses on the initial emissivity (ε_0) along with maximum associated standard deviation. For each MAJIS data, the following information is reported: mean temperature value, mean formal uncertainty associated with the data, 1-sigma dispersion of the data, and maximum temperature value. Units are kelvin.

Observation	**Parameter**	$\varepsilon_0 = 0.7 \pm 0.15$	$\varepsilon_0 = 0.8 \pm 0.20$	$\varepsilon_0 = 0.9 \pm 0.10$	$\varepsilon_0 = 0.95 \pm 0.05$
C1	T_mean	176.3	183.6	184.2	183.3
	σ_formal	22.6	23.3	21.4	19.5
	σ_data	47.5	32.9	34.6	37.6
	T_max	301.6	298.5	295.6	294.2
C2	T_mean	267.2	269.8	269.6	269.4
	σ_formal	2.9	3.2	2.5	1.8
	σ_data	48.8	39.3	40.9	42.1
	T_max	340.1	405.2	340.1	340.1
C3	T_mean	328.0	328.0	328.0	328.0
	σ_formal	0.0	0.0	0.0	0.0
	σ_data	14.7	14.3	14.2	14.2
	T_max	362.3	430.9	365.6	365.7
C4	T_mean	348.6	348.6	348.6	348.6
	σ_formal	0.0	0.0	0.0	0.0
	σ_data	8.9	9.0	9.0	9.0
	T_max	383.1	399.3	382.0	378.8

Code availability. The IDL and Python codes used to retrieve surface temperature and emissivity values are direct implementations of published methods. These scripts were developed independently by specific authors (FT, CR, FC) for internal research purposes, are not publicly released, and may be shared on a case-by-case basis upon justified request.

Data availability. The MAJIS data acquired during the JUICE Moon–Earth flyby in August 2024 are currently under the mission's cruise-phase proprietary period. These data will be made available through the ESA Planetary Science Archive following the first Cruise Archive Delivery, which is currently scheduled for six months after Earth Gravity Assist #3 in 2029. Diviner data are publicly accessible from the NASA Planetary Data System (PDS) Geosciences Node: https://pds-geosciences.wustl.edu/missions/lro/diviner.htm

Author contributions. FT, CR and FC carried out data analysis. FT prepared the manuscript with major contributions from CR and FC. TMP and BTG provided maps derived from Diviner data. FP, AM and FZ contributed to the discussion of results. FP and GP are respectively the PI and Co-PI of the MAJIS instrument. All authors have read and approved the manuscript.

Competing interests. The authors declare that they have no conflict of interest.

Acknowledgements. The authors wish to thank ESA teams from SOC, MOC and ESTEC, as well as Airbus Defence and Space for their technical and operational support to the MAJIS project. JUICE is a mission under ESA leadership with contributions from its Member States, NASA, JAXA and the Israel Space Agency. It is the first Large-class mission in ESA's Cosmic Vision programme.

Financial support. FT, GP, AM, CC and FZ acknowledge support from the Italian Space Agency (ASI), implementation agreement ASI–INAF n. 2023-6-HH.0. CR, FP, YL and CP acknowledge support from the Centre National d'Études Spatiales (CNES), contract CNES–CNRS n° 180 117.

References

Acton, C. H.: Ancillary data services of NASA's Navigation and Ancillary Information Facility, Planet. Space Sci., 44(1), 65–70, https://doi.org/10.1016/0032-0633(95)00107-7, 1996.

Acton, C. H, Bachman, N., Semenov, B., and Wright, E.: A look towards the future in the handling of space science mission geometry, Planet. Space Sci., 150, 9–12, https://doi.org/10.1016/j.pss.2017.02.013, 2018.

Adriani, A., Moriconi, M. L., Mura, A., Tosi, F., Sindoni, G., Noschese, R., Cicchetti, A., and Filacchione, G.: Juno's Earth flyby: the Jovian Infrared Auroral Mapper preliminary results, Astrophys. Space Sci., 361(8), 272, https://doi.org/10.1007/s10509-016-2842-9, 2016.

Adriani, A., Filacchione, G., Di Iorio, T., Turrini, D., Noschese, R., Cicchetti, A., Grassi, D., Mura, A., Sindoni, G., Zambelli, M., Piccioni, G., Capria, M. T., Tosi, F., Orosei, R., Dinelli, B. M., Moriconi, M. L., Roncon, E., Lunine, J. I., Becker, H. N., Bini, A., Barbis, A., Calamai, L., Pasqui, C., Nencioni, S., Rossi, M., Lastri, M., Formaro, R., and Olivieri, A.: JIRAM, the Jovian Infrared Auroral Mapper, Space Sci. Rev., 213(1–4), 393–446, https://doi.org/10.1007/s11214-014-0094-y, 2017.

Bandfield, J. L., Hayne, P. O., Williams, J.-P., Greenhagen, B. T., and Paige, D. A.: Lunar surface roughness derived from LRO Diviner Radiometer observations, Icarus, 248, 357–372, https://doi.org/10.1016/j.icarus.2014.11.009, 2015.

Bandfield, J. L., Poston, M. J., Klima, R. L., and Edwards, C. S.: Widespread distribution of OH/H2O on the lunar surface inferred from spectral data, Nat. Geosci., 11(3), 173–177, https://doi.org/10.1038/s41561-018-0065-0, 2018.

Bellucci, G., Brown, R. H., Formisano, V., Baines, K. H., Bibring, J.-P., Buratti, B. J., Capaccioni, F., Cerroni, P., Clark, R. N., Coradini, A., Cruikshank, D. P., Drossart, P., Jaumann, R., Langevin, Y., Matson, D. L., McCord, T. B., Mennella, V., Miller, E., Nelson, R. M., Nicholson, P. D., Sicardy, B., and Sotin, C.: Cassini/VIMS observations of the moon, Adv. Space Res., 30(8), 1889–1894, https://doi.org/10.1016/S0273-1177(02)00484-2, 2002.

Brown, R. H., Baines, K. H., Bellucci, G., Bibring, J.-P., Buratti, B. J., Capaccioni, F., Cerroni, P., Clark, R. N., Coradini, A., Cruikshank, D. P., Drossart, P., Formisano, V., Jaumann, R., Langevin, Y., Matson, D. L., McCord, T. B., Mennella, V., Miller, E., Nelson, R. M., Nicholson, P. D., Sicardy, B., and Sotin, C.: The Cassini Visual And Infrared Mapping Spectrometer (VIMS) Investigation, Space Sci. Rev., 115(1–4), 111–168, https://doi.org/10.1007/s11214-004-1453-x, 2004.

Capria, M. T., Tosi, F., De Sanctis, M. C., Capaccioni, F., Ammannito, E., Frigeri, A., Zambon, F., Fonte, S., Palomba, E., Turrini, D., Titus, T. N., Schröder, S. E., Toplis, M., Li, J.-Y., Combe, J.-Ph., Raymond, C. A., and Russell, C. T.: Vesta surface thermal properties map, Geophys. Res. Lett., 41(5), 1438–1443, https://doi.org/10.1002/2013GL059026, 2014.

Chowdhury, A. R., Banerjee, A., Joshi, S. R., Dutta, M., Kumar, A., Bhattacharya, S., Amitabh, Rehman, S. U., Bhati, S., Karelia, J. C., Biswas, A., Saxena, A. R., Sharma, S., Somani, S. R., Bhagat, H. V., Sharma, J., Ghonia, D. N., Bokarwadia, B. B., and Parasar, A.: Imaging Infrared Spectrometer onboard Chandrayaan-2 Orbiter, Curr. Sci., 118(3), 368–375, https://doi.org/10.18520/cs/v118/i3/368-375, 2020.

Christensen, P. R., Hamilton, V. E., Anwar, S., Mehall, G., Spencer, J. R., Sunshine, J. M., and Levison, H. F.: Thermal Infrared Spectra of the Moon: Results From the Lucy Thermal Emission Spectrometer Observations, J. Geophys. Res. Planets, 130(5), e2024JE008493, https://doi.org/10.1029/2024JE008493, 2025.

Davidsson, B. J. R. and Rickman, H.: Surface roughness and three-dimensional heat conduction in thermophysical models, Icarus, 243, 58–77, https://doi.org/10.1016/j.icarus.2014.08.039, 2014.

Donaldson Hanna, K. L., Thomas, I. R., Bowles, N. E., Greenhagen, B. T., Pieters, C. M., Mustard, J. F., Jackson, C. R. M., and Wyatt, M. B.: Laboratory emissivity measurements of the plagioclase solid solution series under varying environmental conditions, J. Geophys. Res., 117(E11), E11004, https://doi.org/10.1029/2012JE004184, 2012.

Grasset, O., Dougherty, M. K., Coustenis, A., Bunce, E. J., Erd, C., Titov, D., Blanc, M., Coates, A., Drossart, P., Fletcher, L. N., Hussmann, H., Jaumann, R., Krupp, N., Lebreton, J.-P., Prieto-Ballesteros, O., Tortora, P., Tosi, F., and Van Hoolst, T.: JUpiter ICy moons Explorer (JUICE): An ESA mission to orbit Ganymede and to characterise the Jupiter system, Planet. Space Sci., 78, 1–21, https://doi.org/10.1016/j.pss.2012.12.002, 2013.

Greenhagen, B. T., Lucey, P. G., Wyatt, M. B., Glotch, T. D., Allen, C. C., Arnold, J. A., Bandfield, J. L., Bowles, N. E., Donaldson Hanna, K. L., Hayne, P. O., Song, E., Thomas, I. R., and Paige, D. A.: Global Silicate Mineralogy of the Moon from the Diviner Lunar Radiometer, Science, 329(5998), 1507–1509 , https://doi.org/10.1126/science.1192196, 2010.

Guerlet, S., Armante, R., Lauzanne, N., Poulet, F., Langevin, Y., Rodriguez, S., Fletcher, L., Fouchet, L., Piccioni, G., and Migliorini, A.: MAJIS performances in the infrared during the JUICE 2024 Earth fly-by: comparisons with IASI measurements and sensitivity to trace species, Ann. Geophys., this issue, https://doi.org/10.5194/egusphere-2026-805, 2026.

Haffoud, P., Poulet, F., Vincendon, M., Filacchione, G., Barbis, A., Guiot, P., Lecomte, B., Langevin, Y., Piccioni, G., Dumesnil, C., Rodriguez, S., Carter, J., Stefani, S., Tommasi, L., Tosi, F., and Pilorget, C.: Calibration of MAJIS (Moons And Jupiter Imaging Spectrometer). III. Spectral calibration, Rev. Sci. Instrum., 95(3), 031301, https://doi.org/10.1063/5.0188944, 2024.

Hapke, B.: Bidirectional reflectance spectroscopy. I – Theory, J. Geophys. Res., 86(B4), 3039–3054, https://doi.org/10.1029/JB086iB04p03039, 1981.

Hapke, B.: Theory of Reflectance and Emittance Spectroscopy, Cambridge Univ. Press, New York, 2005.

Keihm, S. J., Peters, K., Langseth, M. G., and Chute, J. L.: Apollo 15 measurement of lunar surface brightness temperatures: Thermal conductivity of the upper 1½ meters of regolith, Earth Planet. Sci. Lett., 19(3), 337–351, https://doi.org/10.1016/0012-821X(73)90084-8, 1973.

Keihm, S. J. and Langseth, M. G.: Lunar Microwave Brightness Temperature Observations Reevaluated in the Light of Apollo Program Findings, Icarus, 24(2), 211–230, https://doi.org/10.1016/0019-1035(75)90100-1, 1975.

Keihm, S., Tosi, F., Kamp, L., Capaccioni, F., Gulkis, S., Grassi, D., Hofstadter, M., Filacchione, G., Lee, S., Giuppi, S., Janssen, M., and Capria, M. T.: Interpretation of combined infrared, submillimeter, and millimeter thermal flux data obtained during the Rosetta fly-by of Asteroid (21) Lutetia, Icarus, 221(1), 395–404, https://doi.org/10.1016/j.icarus.2012.08.002, 2012.

Langevin, Y., Rodriguez, S., Guerlet, S., Poulet, F., Piccioni, G., Agostini, L., Armante, R., D'Aversa, E., Filacchione, G., Fletcher, L., Oliva, F., Royer, C., Seignovert, B., Stephan, K., Tosi, F., and Trent, T.: Post launch spectral and radiometric performances of MAJIS, the VIS-NIR imaging spectrometer of JUICE, Ann. Geophys., this issue, doi: 10.5194/egusphere-2026-410, 2026.

Li, S. and Li, L.: Radiative transfer modeling for quantifying lunar surface minerals, particle size, and submicroscopic metallic Fe, J. Geophys. Res., 116(E9), E09001, https://doi.org/10.1029/2011JE003837, 2011.

Li, S. and Milliken, R. E.: An empirical thermal correction model for Moon Mineralogy Mapper data constrained by laboratory spectra and Diviner temperatures, J. Geophys. Res. Planets, 121(10), 2081–2107, https://doi.org/10.1002/2016JE005035, 2016.

Lommel, E. C. G: "Die Photometrie der diffusen Zurückwerfung", Sitzungsber. d. math. phys. Class d. K. B. Acad. zu München, 17, 95–132, 1887.

Müller, T. G., Burgdorf, M., Alí-Lagoa, V., Buehler, S. A., and Prange, M.: The Moon at thermal infrared wavelengths: a benchmark for asteroid thermal models, Astron. Astrophys., 650, A38, https://doi.org/10.1051/0004-6361/202039946, 2021.

Mustard, J. F. and Hays, J. E.: Effects of hyperfine particles on reflectance spectra from 0.3 to 25 μm, Icarus, 125(1), 145–163, https://doi.org/10.1006/icar.1996.5583, 1997.

Ojha, S. P., Dagar, A. K., Vikram, K. V. N. G., Bhattacharya, S., Bhattacharya, B. K., and Kiran Kumar, A. S.: Simultaneous physical retrieval of daytime lunar surface temperature and spectral emissivity in the 3–5 μm range from Chandrayaan-2 IIRS observations, Curr. Sci., 126(7), 781–790, https://doi.org/10.18520/cs/v126/i7/781-790, 2024.

Poulet, F., Piccioni, G., Langevin, Y., Dumesnil, C., Tommasi, L., Carlier, V., Filacchione, G., Amoroso, M., Arondel, A., D'Aversa, E., Barbis, A., Bini, A., Bolsée, D., Bousquet, P., Caprini, C., Carter, J., Dubois, J.-P., Condamin, M., Couturier, S., Dassas, K., Dexet, M., Fletcher, L., Grassi, D., Guerri, I., Haffoud, P., Larigauderie, C., Le Du, M., Mugnuolo, R., Pilato, G., Rossi, M., Stefani, S., Tosi, F., Vincendon, M., Zambelli, M., Arnold, G., Bibring, J.-P., Biondi, D., Boccaccini, A., Brunetto, R., Carapelle, A., Cisneros González, M., Hannou, C., Karatekin, O., Le Cle'ch, J.-C., Leyrat, C., Migliorini, A., Nathues, A., Rodriguez, S., Saggin, B., Sanchez-Lavega, A., Schmitt, B., Seignovert, B., Sordini, R., Stephan, K., Tobie, G., Zambon, F., Adriani, A., Altieri, F., Bockelée-Morvan, D., Capaccioni, F., De Angelis, S., De Sanctis, M.-C., Drossart, P., Fouchet, T., Gérard, J.-C., Grodent, D., Ignatiev, N., Irwin, P., Ligier, N., Manaud, N., Mangold, N., Mura, A., Pilorget, C., Quirico, E., Renotte, E., Strazzulla, G., Turrini, D., Vandaele, A.-C., Carli, C., Ciarniello, M., Guerlet, S., Lellouch, E., Mancarella, F., Morbidelli, A., Le Mouélic, S., Raponi, A., Sindoni, G., and Snels, M.: Moons and Jupiter Imaging Spectrometer (MAJIS) on Jupiter Icy Moons Explorer (JUICE), Space Sci. Rev., 220(3), 27, https://doi.org/10.1007/s11214-024-01057-2, 2024.

Poulet, F., Piccioni, G., Langevin, Y., Dumesnil, C., Carlier, V., Seignovert, B., Dexet, M., Fletcher, L. N., Leyrat, C., Altieri, F., Carter, J., D'Aversa, E., De Sanctis, M. C., Grassi, D., Guerlet, S., Le Mouélic, S., Migliorini, A., Oliva, F., Royer, C., Rodriguez, S., Stephan, K., Tosi, F., Zambon, F., Adriani, A., Arnold, G., Bibring, J.-P., Bockelée-Morvan, D., Brunetto, R., Capaccioni, F., Carli, C., Cavalié, T., Cisneros González, M., Ciarnello, M., De Angelis, M., Drossart, P., Filacchione, G., Fouchet, T., Gérard, J.-C., Grodent, D., Irwin, P., Jacquinod, S., Karatekin, O., Lellouch, E., Ligier, N., Mangold, N., Mebsout, M., Merlin, F., Morbidelli, A., Mura, A., Nathues, A., Palumbo, M. E., Pilorget, C., Poch, O., Quirico, E., Raponi, A., Robert, S., Roussos, E., Sanchez-Lavega, A., Schmitt, B., Sindoni, G., Snels, M., Sordini, R., Stefani, S., Strazzulla, G., Trent, T., Tobie, G., Turrini, D., Vandaele, A.-C., Vincendon, M., Witasse, O., Vallat, C., and Moirano, A.: ESA/JUICE encounters Earth/Moon in 2024: Overview of the Moons And Jupiter Imaging Spectrometer (MAJIS) observations, Ann. Geophys., this issue, https://doi.org/10.5194/angeo-44-163-2026, 2026.

Paige, D. A., Foote, M. C., Greenhagen, B. T., Schofield, J. T., Calcutt, S., Vasavada, A. R., Preston, D. J., Taylor, F. W., Allen, C. C., Snook, K. J., Jakosky, B. M., Murray, B. C., Soderblom, L. A., Jau, B., Loring, S., Bulharowski, J., Bowles, N. E., Thomas, I. R., Sullivan, M. T., Avis, C., de Jong, E. M., Hartford, W., and McCleese, D. J.: The Lunar Reconnaissance Orbiter Diviner Lunar Radiometer Experiment, Space Sci. Rev., 150(1–4), 125–160, https://doi.org/10.1007/s11214-009-9529-2, 2010.

Ren, H., Nie, J., Dong, J., Liu, R., Fa, W., Hu, L., and Fan, W.: Lunar Surface Temperature and Emissivity Retrieval From Diviner Lunar Radiometer Experiment Sensor, Earth Space Sci., 8(1), e01436, https://doi.org/10.1029/2020EA001436, 2021.

Rodgers, C. D.: Inverse Methods for Atmospheric Sounding – Theory and practice, World Scientific Publishing Co., Singapore, Series on Atmospheric, Oceanic and Planetary Physics – Vol. 2, https://doi.org/10.1142/3171, ISBN: 978-981-02-2740-1, 2000.

Royer, C., Haffoud, P., Langevin, Y., Poulet, F., Bockelée-Morvan, D., D'Aversa, E., Cisneros-González, M., Grassi, D., Ligier, N., Piccioni, G., Carter, J., Tosi, F., Vincendon, M., Zambon, F., Zakharov, V., Gilles, M., and Seignovert, B.: A simulator of the MAJIS instrument onboard the JUICE mission: Description and application to operational and scientific cases, Planet. Space Sci., 264, 106147, https://doi.org/10.1016/j.pss.2025.106147, 2025.

Rozitis, B. and Green, S. F.: Directional characteristics of thermal-infrared beaming from atmosphereless planetary surfaces - a new thermophysical model, Mon. Not. R. Astron. Soc., 415(3), 2042–2062, https://doi.org/10.1111/j.1365-2966.2011.18718.x, 2011.

Rozitis, B., Emery, J. P., Siegler, M. A., Susorney, H. C. M., Molaro, J. L., Hergenrother, C. W., and Lauretta, D. S.: Implications for Ice Stability and Particle Ejection From High-Resolution Temperature Modeling of Asteroid (101955) Bennu, J. Geophys. Res., 116, E09001, https://doi.org/10.1029/2019JE006323, 2020.

Rubanenko, L., Schorghofer, N., Greenhagen, B. T., and Paige, D. A.: Equilibrium Temperatures and Directional Emissivity of Sunlit Airless Surfaces With Applications to the Moon, J. Geophys. Res., 125(6), https://doi.org/10.1029/2020JE006377, 2020.

Seeliger, H.: Zur Theorie Baleuchtung der Grossen Planeten Inbesondere des Saturn, Abhandl. Bayer. Akad. Wiss. Math. Naturw. Kl. II, 16, 405–516, 1888.

Salisbury, J. W., Walter, L. S. and Vergo, N: Mid-infrared (2.1–25 μm) reflectance spectra of powdered lunar soils and rock chips, U.S. Geological Survey, Open-File Report 87–263, https://pubs.usgs.gov/of/1987/0263/report.pdf, 1987.

Salisbury, J. W., Basu, A., and Fischer, E. M.: Thermal Infrared Spectra of Lunar Soils, Icarus, 130(1), 125–139, https://doi.org/10.1006/icar.1997.5809, 1997.

Seignovert, B., Poulet, F., Langevin, Y., D'Aversa, E., Ligier, N., Dumesnil, C., Mesbout, M., Leyrat, C., Jacquinod, S., Le Mouélic, S., Tobie, G., Mangold, N., Piccioni, G., Tosi, F., Stephan, K., Palumbo, P., Agostini, L., Penasa, L., Le Deit, L., Cornet, T., Belgacem, I., Costa-Sitja, M., Escalante Lopez, A., and Schmauß, S.: Geometric in-flight calibration of MAJIS (JUICE) during early cruise phase and LEGA flyby, Ann. Geophys., this issue, https://doi.org/10.5194/egusphere-2026-2655, 2026.

Shkuratov, Y., Kaydash, V., Korokhin, V., Velikodsky, Y., Opanasenko, N., and Videen, G.: Optical measurements of the Moon as a tool to study its surface, Planet. Space Sci., 59(13), 1326–1371, https://doi.org/10.1016/j.pss.2011.06.011, 2011.

Smith, D. E., Zuber, M. T., Neumann, G. A., Lemoine, F. G., Mazarico, E., Torrence, M., McGarry, J. F., Rowlands, D. D., Head, J. W., Duxbury, T. H., Aharonson, O., Lucey, P. G, Robinson, M. S., Barnouin, O. S., Cavanaugh, J. F., Sun, X., Liiva, P., Mao, D., Smith, J. C., and Bartels, A. E.: Initial observations from the Lunar Orbiter Laser Altimeter (LOLA), Geophys. Res. Lett., 37(18), L18204, https://doi.org/10.1029/2010GL043751, 2010.

Smith, D. E., Zuber, M. T., Neumann, G. A., Mazarico, E., Lemoine, F. G., Head, J. W., III, Lucey, P. G., Aharonson, O., Robinson, M., S., Sun, X., Torrence, M., H., Barker, M. K., Oberst, J., Duxbury, T. C., Mao, D. Barnouin, O. S., Jha, K., Rowlands, D. D., Goossens, S., Baker, D. Bauer, S., Gläser, P., Lemelin, M., Rosenburg, M., Sori, M. M., Whitten, J., and McLanahan, T.: Summary of the results from the lunar orbiter laser altimeter after seven years in lunar orbit, Icarus, 283, 70–91, https://doi.org/10.1016/j.icarus.2016.06.006, 2017.

Spencer, J. R.: A rough-surface thermophysical model for airless planets, Icarus, 83(1), 27–38, https://doi.org/10.1016/0019-1035(90)90004-S, 1990.

Speyerer, E. J., Robinson, M. S., Denevi, B. W., and LROC Science Team (2011). Lunar Reconnaissance Orbiter Camera global morphological map of the Moon, Paper presented at the 42nd Lunar Planetary Science Conference, Lunar and Planetary Science Institute, Houston, TX. https://www.lpi.usra.edu/meetings/lpsc2011/pdf/2387.pdf

Tosi, F., Capria, M. T., De Sanctis, M. C., Combe, J.-Ph., Zambon, F., Nathues, A., Schröder, S. E., Li, J.-Y., Palomba, E., Longobardo, A., Blewett, D. T., Denevi, B. W., Palmer, E., Capaccioni, F., Ammannito, E., Titus, T. M., Mittlefehldt, D. W., Sunshine, J. M., Russell, C. T., and Raymond, C. A.: Thermal measurements of dark and bright surface features on Vesta as derived from Dawn/VIR, Icarus, 240, 36–57, https://doi.org/10.1016/j.icarus.2014.03.017, 2014.

Tosi, F., Frigeri, A., Combe, J.-Ph., Zambon, F., De Sanctis, M. C., Ammannito, E., Longobardo, A., Hoffmann, M., Nathues, A., Garry, W. B., Blewett, D. T., Pieters, C. M., Palomba, E., Stephan, K., McFadden, L. A., McSween, H. Y., Russell, C. T., and Raymond, C. A.: Mineralogical analysis of the Oppia quadrangle of asteroid (4) Vesta: Evidence for occurrence of moderate-reflectance hydrated minerals, Icarus, 259, 129–149, https://doi.org/10.1016/j.icarus.2015.05.018, 2015.

Tosi, F., Carrozzo, F. G., Raponi, A., De Sanctis, M. C., Thangjam, G., Zambon, F., Ciarniello, M., Nathues, A., Capria, M. T., Rognini, E., Ammannito, E., Hoffmann, M., Krohn, K., Longobardo, A., Palomba, E., Pieters, C. M., Stephan, K., Raymond, C. A., and Russell, C. T.: Mineralogy and temperature of crater Haulani on Ceres, Meteorit. Planet. Sci., 53(9), 1902–1924, https://doi.org/10.1111/maps.13078, 2018.

Tosi, F., Capaccioni, F., Capria, M. T., Mottola, S., Zinzi, A., Ciarniello, M., Filacchione, G., Hofstadter, M., Fonti, S., Formisano, M., Kappel, D., Kührt, E., Leyrat, C., Vincent, J.-B., Arnold, G., De Sanctis, M. C., Longobardo, A., Palomba, E., Raponi, A., Rousseau, B., Schmitt, B., Barucci, M. A., Bellucci, G., Benkhoff, J., Bockelée-Morvan, D., Cerroni, P., Combe, J.-Ph., Despan, D., Erard, S., Mancarella, F., McCord, T. B., Migliorini, A., Orofino, V., and Piccioni, G.: The changing temperature of the nucleus of comet 67P induced by morphological and seasonal effects, Nat. Astron., 3(7), 649–658, https://doi.org/10.1038/s41550-019-0740-0, 2019.

Tosi, F., Roatsch, T., Galli, A., Hauber, E., Lucchetti, A., Molyneux, P., Stephan, K., Achilleos, N., Bovolo, F., Carter, J., Cavalié, T., Cimò, G., D'Aversa, E., Gwinner, K., Hartogh, P., Huybrighs, H., Langevin, Y., Lellouch, E., Migliorini, A., Palumbo, P., Piccioni, G., Plaut, J. J., Postberg, F., Poulet, F., Retherford, K., Rezac, L., Roth, L., Solomonidou, A., Tobie, G., Tortora, P., Tubiana, C., Wagner, R., Wirström, E., Wurz, P., Zambon, F., Zannoni, M., Barabash, S., Bruzzone, L., Dougherty, M., Gladstone, R., Gurvits, L. I., Hussmann, H., Iess, L., Wahlund, J.-E., Witasse, O., Vallat, C., and Lorente, R.: Characterization of the Surfaces and Near-Surface Atmospheres of Ganymede, Europa and Callisto by JUICE, Space Sci. Rev., 220(5), 59, https://doi.org/10.1007/s11214-024-01089-8, 2024.

Vasavada, A. R., Paige, D. A., and Wood, S. E.: Near-Surface Temperatures on Mercury and the Moon and the Stability of Polar Ice Deposits, Icarus, 141(2), 179–193, https://doi.org/10.1006/icar.1999.6175, 1999.

Vasavada, A. R., Bandfield, J. L., Greenhagen, B. T., Hayne, P. O., Siegler, M. A., Williams, J.-P., and Paige, D. A.: Lunar equatorial surface temperatures and regolith properties from the Diviner Lunar Radiometer Experiment, J. Geophys. Res., 117(E12), E00H18, https://doi.org/10.1029/2011JE003987, 2012.

Verma, P. A, Chauhan, M., and Chauhan, P.: Lunar surface temperature estimation and thermal emission correction using Chandrayaan-2 imaging infrared spectrometer data for H2O & OH detection using 3 μm hydration feature, Icarus, 383, https://doi.org/10.1016/j.icarus.2022.115075, 2022.

Wagner, R. V., Speyerer, E. J., Robinson, M. S., and LROC Team (2015): New Mosaicked Data Products from the LROC Team, Paper presented at the 46th Lunar and Planetary Science Conference, Lunar and Planetary Institute, Houston, TX. https://www.hou.usra.edu/meetings/lpsc2015/pdf/1473.pdf

Williams, J.-P., Paige, D. A., Greenhagen, B. T., and Sefton-Nash, E.: The global surface temperatures of the Moon as measured by the Diviner Lunar Radiometer Experiment, Icarus, 283, 300–325, https://doi.org/10.1016/j.icarus.2016.08.012, 2017.

Williams, J.-P., Bandfield, J. L., Paige, D. A., Powell, T. M., Greenhagen, B. T., Taylor, S., Hayne, P. O., Speyerer, E. J., Ghent, R. R., and Costello, E. S.: Lunar cold spots and crater production on the Moon, J. Geophys. Res. Planets, 123(9), 2380–2392, https://doi.org/10.1029/2018JE005652, 2018.

Wöhler, C., Grumpe, A., Berezhnoy, A. A., and Shevchenko, V. V.: Time-of-day–dependent global distribution of lunar surficial water/hydroxyl, Sci. Adv., 3(9), https://doi.org/10.1126/sciadv.1701286, 2017.

Wohlfarth, K., Wöhler, C., Hiesinger, H., and Helbert, J.: An advanced thermal roughness model for airless planetary bodies. Implications for global variations of lunar hydration and mineralogical mapping of Mercury with the MERTIS spectrometer, Astron. Astrophys., 674, A69, https://doi.org/10.1051/0004-6361/202245343, 2023.

Wu, Y., Meng, Z., Liu, Y., Huang, J., Zou, Y., Tang, X., Jiang, X., and Wang, Z.: Unveiling the secrets of the midinfrared (3.5 μm) Moon: First global lunar image of a single exposure, Geophys. Res. Lett., 48(4), e2020GL0883, https://doi.org/10.1029/2020GL088393, 2021.

Zambon, F., Altieri, F., De Sanctis, M. C., Le Mouélic, S., Piccioni, G., Poulet, F., Langevin, Y., Royer, C., Tosi, F., Karatekin, O., Mura, A., and Carli, C.: Spectral analyzes of lunar regions observed by MAJIS during the JUICE Earth-Moon flyby, Ann. Geophys., this issue, https://doi.org/10.5194/egusphere-2026-876, 2026.